Computers and Geotechnics 201 (2027) 108547

Contents lists available at ScienceDirect

Computers and Geotechnics

journal homepage: www.elsevier.com/locate/compgeo

Research Paper

Unveiling anisotropic elasticity of granular materials under true triaxial conditions

Hechen Zhou [a], Xiaoqiang Gu [a,b,*], Hai-Lin Wang [a,c], Xiaomin Liang [a,d]

[a] Department of Geotechnical Engineering, Tongji University, Shanghai, China
[b] School of Civil Engineering and Architecture, Zhejiang Sci-Tech University, Zhejiang, China
[c] Department of Civil and Environmental Engineering, The Hong Kong Polytechnic University, Hong Kong, China
[d] School of Safety Science and Engineering, Nanjing University of Science and Technology, Nanjing, China

ARTICLE INFO

Keywords:
DEM
Anisotropic elasticity
True triaxial condition
Young's modulus
Micromechanics

ABSTRACT

How to characterize the directional elastic constants of granular materials under true triaxial stress states remains an open issue, since anisotropic elasticity is governed by the interplay between inherent anisotropy and stress-induced anisotropy. This study addresses the issue through discrete element method (DEM) probe tests on sphere and clump assemblies under various true triaxial stress states. The three directional Young's moduli and six Poisson's ratios are first obtained from DEM simulations. An orthotropic hyperelastic formulation is developed to derive explicit expressions for anisotropic elasticity. The scalar stiffness parameters K and G, closely correlated with the mechanical coordination number, govern the magnitude of the elastic constants, whereas the elastic fabric tensor **a** describes the directional contrast. Based on the kinematic hypothesis, two new micromechanical tensors are proposed to incorporate the combined effects of interparticle contact stiffness, branch vector and contact normal. These tensors establish an explicit link between anisotropic elasticity and the underlying microstructure. The theoretical predictions show good agreement with the DEM results and provide a physically interpretable means of deciphering anisotropic elasticity under true triaxial conditions.

1. Introduction

At strains below approximately 0.001 %, soils are generally considered to behave in an elastic manner (Clayton, 2011). A sound characterization of elasticity is therefore fundamental to geotechnical analysis and design, as the strains encountered in many engineering applications lie predominantly within the small-to-medium strain range, where accurate prediction of deformation and ground movements is crucial for the serviceability of nearby structures and buried infrastructure (Castellón and Ledesma, 2022).

The elastic behavior of soils is seldom isotropic. Owing to depositional history, particle morphology and particle arrangement, natural soils commonly exhibit inherent anisotropy (Yimsiri and Soga, 2011), which may be further modified by external loading to produce stress-induced anisotropy (Bellotti et al., 1996). Experimental studies using bender element tests (Dutta et al., 2020), resonant column tests (Payan et al., 2017), triaxial tests (Kuwano and Jardine, 2007) and hollow cylinder apparatus tests (Gasparre et al., 2007) have provided important insights into anisotropic elastic properties. Ezaoui and Di Benedetto (2009) showed that the Young's modulus E_i in a given direction depends mainly on the stress in that direction, leading to the following expression (Hoque and Tatsuoka, 2004):

$$E_i = A_i F(e) \left(\frac{\sigma_i}{p_a}\right)^{m_i} \tag{1}$$

where A_i is a directional constant depending on soil type, σ_i refers to the effective stress in the i direction, p_a denotes a reference stress, m_i is an exponent reflecting the influence of effective stress and $F(e)$ is a function of void ratio, expressed as $F(e) = (2.17\text{-}e)^2/(1+e)$ (Hardin and Richart, 1963). However, this unique stress-dependence may not hold at large stress ratio (SR) owing to fabric damage induced by loading (Hoque and Tatsuoka, 2004). Particle gradation and particle shape may also affect E_i through the directional parameters A_i and m_i (Payan et al., 2017). Although many studies have examined cross-anisotropic elasticity under axisymmetric conditions (Bellotti et al., 1996; Lings et al., 2000; Kuwano and Jardine, 2002; Gasparre et al., 2007), soils in engineering practice often experience more general stress states. Hence, the anisotropic elasticity of granular materials should be examined under these

* Corresponding author.
E-mail address: guxiaoqiang@tongji.edu.cn (X. Gu).

https://doi.org/10.1016/j.compgeo.2026.108547
Received 21 May 2026; Received in revised form 27 July 2026; Accepted 11 August 2026
Available online 18 August 2026
0266-352X/

more complex conditions. Callisto and Rampello (2002) investigated the strength envelope under true triaxial loading and the degradation of shear modulus along different loading paths. Nevertheless, the anisotropic elasticity of granular materials under true triaxial stress states remains insufficiently understood, particularly with respect to the directional differences among Young's moduli and Poisson's ratios.

A major limitation of experimental investigations is the difficulty of measuring elastic strains with sufficient accuracy. At very small strain levels, the precise determination of strain is challenging and the Poisson's-ratio terms are susceptible to measurement errors (Gasparre et al., 2007; Suwal and Kuwano, 2013). Moreover, experiments provide limited access to particle-scale mechanisms, such as contact arrangement, fabric evolution and contact interaction.

The discrete element method (DEM) proposed by Cundall and Strack (1979) offers a useful tool for examining these mechanisms. In DEM, elastic response is commonly evaluated by probe tests. As suggested by Cundall et al. (1989), the interparticle friction coefficient is assigned a sufficiently large value to suppress contact sliding, so that the simulated response remains elastic. Gu et al. (2013, 2017) performed probe tests on cross-anisotropic granular assemblies. Their results showed that the Young's modulus in a given direction depends on the stress acting in that direction when *SR* is within a threshold value. Beyond this threshold, E_i decreases owing to a decline in the contact number. Gu et al. (2024) quantified fabric anisotropy using wave velocity, showing that fabric anisotropy is linearly related to the ratio of stress-normalized wave velocities. However, their study was restricted to spherical assemblies. Jiang and Yang (2024) indicated that E_i is influenced not only by σ_i but also by *SR* and introduced a new factor into Eq. (1). Singh and Buscarnera (2024, 2025) introduced a contact area fabric tensor and showed that elastic anisotropy can be disentangled into contributions from shape fabric and contact area fabric. Chen et al. (2026) examined the relationship between elastic anisotropy and contact normal fabric invariants. Nonetheless, their study was confined to conventional triaxial stress states. In addition, some DEM studies have investigated granular behavior under true triaxial loading at large strains, focusing on the effects of loading path, interparticle friction, particle size and particle shape on the true triaxial strength envelope, peak strength and fabric evolution (Shi and Guo, 2018; Liu et al., 2020; Wen and Zhang, 2022; Zhou et al., 2022; Irani et al., 2024; Liu and Yan, 2025). To the best of the authors' knowledge, the anisotropic elasticity under true triaxial stress states has not yet been systematically elucidated, particularly regarding the interplay between inherent anisotropy and stress-induced anisotropy.

Another important route is provided by micromechanical approaches. Since granular materials can be regarded as assemblies of discrete particles, their macroscopic behavior can be derived from particle-scale quantities, including the geometric arrangement of the contact network (e.g. contact normal fabric and branch vector fabric) and the force–displacement relations at contacts. In this way, micromechanical methods offer a rational means of linking the macroscopic response to the underlying microstructure. Two main hypotheses are commonly used to establish the micro–macro connection, namely the static hypothesis and the kinematic hypothesis (Chang et al., 1995; Liao et al., 1997). Under the static hypothesis, the average stress of a granular assembly is related to an averaged field of contact forces. Since particle-scale equilibrium is not necessarily satisfied throughout the representative volume, the resulting constitutive tensor is a lower estimate rather than a rigorous lower bound. The kinematic hypothesis assumes that all particles deform in accordance with a uniform deformation field, which leads to an upper-bound solution owing to the kinematic constraint imposed on the system. Based on these two hypotheses, Chang et al. (1995) derived corresponding expressions for the elastic Young's modulus:

$$E_{\text{static}} = \frac{20N_c r^2 k_n}{3V}\left(\frac{\alpha}{2+3\alpha}\right) \tag{2}$$

$$E_{\text{kinematic}} = \frac{4N_c r^2 k_n}{3V}\left(\frac{2+3\alpha}{4+\alpha}\right) \tag{3}$$

where $\alpha = k_s/k_n$, k_n and k_s are the normal and tangential contact stiffnesses, respectively, N_c is the total number of interparticle contacts within the representative volume V, and r is the particle radius. It should be noted that Eqs. (2)-(3) are derived for spherical particles of identical size. Based on the static hypothesis and the Hertz-Mindlin contact model (Mindlin and Deresiewicz, 1953), Yimsiri and Soga (2000) obtained an explicit analytical solution for the Young's modulus of spherical assemblies under isotropic stress conditions:

$$E = \frac{20r^2}{(5-4\nu_g)}\left(\frac{N_c G_g}{V}\right)^{2/3}\left[\frac{(1-\nu_g)\sigma_c}{6}\right]^{1/3} \tag{4}$$

where G_g and υ_g are the particle shear modulus and Poisson's ratio, respectively, σ_c denotes the confining pressure.

Hicher and Chang (2005) further compared the predictions of the kinematic and static hypotheses, both combined with the Hertz-Mindlin model, against experimental results. They highlighted that natural sands are composed of particles with irregular shapes and therefore do not behave as assemblies of ideal elastic spheres. To account for this, they introduced corrections through the contact stiffness ratio, $\alpha = k_s/k_n$, together with the initial contact normal fabric, so that the theoretical predictions could reproduce the experimental observations. Nevertheless, their formulation was based on spherical assemblies and did not explicitly incorporate branch vector, which may be indispensable for considering particle shape effects. In a similar vein, Otsubo et al. (2025) proposed a micromechanical expression for the elastic shear modulus of non-spherical particles by introducing an empirically modified coefficient to account for particle shape effects. Recently, the role of particle rotation has received increasing attention. Agnolin and Roux (2008) found that particle rotation induces tangential fluctuations, which in turn affect the theoretical estimation of elastic behavior. Kruyt et al. (2010) noted that particle rotations are difficult to predict accurately because of their strong sensitivity to contact geometry. Fleischmann et al. (2013a, 2013b) demonstrated that particle rotation must be properly accounted for to reproduce the elastic response observed in DEM simulations. They introduced an internal parameter ζ, leading to an effective tangential stiffness $k_s{}^* = \zeta k_s$, to incorporate the influence of particle rotation. However, existing micromechanical approaches have not yet been extended to characterize anisotropic elasticity under true triaxial stress states.

In this study, DEM probe tests were carried out on specimens with spherical and non-spherical particles under a range of true triaxial stress states. The corresponding directional Young's moduli and Poisson's ratios were determined. A hyperelastic formulation was then developed to derive explicit expressions for these elastic constants. Based on the kinematic hypothesis, two new micromechanical tensors were introduced, through which the specimen anisotropy could be directly related to its underlying microstructure. By combining the hyperelastic formulation with the micromechanical descriptors, the anisotropic elasticity of granular materials under true triaxial conditions was quantitatively characterized, and the predictions were found to agree well with the DEM results.

2. DEM modelling

2.1. Specimen generation

DEM simulations were performed using PFC3D. To reproduce the stress dependence of elastic stiffness, particle–particle interactions were governed by a simplified Hertz-Mindlin law, in which both the normal and tangential contact stiffnesses vary with the normal contact force. The expressions for k_n and k_s are given by Mindlin and Deresiewicz (1953):

$$k_n = \frac{3}{4}\left[\frac{8G_g}{3(1-\nu_g)}\right]^{2/3}\bar{r}^{1/3}N^{1/3} = C_n\bar{r}^{1/3}N^{1/3} \quad (5)$$

$$k_s = \frac{2\left[3(G_g)^2(1-\nu_g)\right]^{1/3}}{2-\nu_g}\bar{r}^{1/3}N^{1/3} = C_s\bar{r}^{1/3}N^{1/3} \quad (6)$$

where G_g and υ_g are the particle shear modulus and Poisson's ratio, respectively, N is the normal contact force, C_n and C_s denote the corresponding coefficient terms, and $\bar{r}$ is the effective contact radius, which is evaluated as:

$$\frac{1}{\bar{r}} = \frac{1}{2}\left(\frac{1}{r_i} + \frac{1}{r_j}\right) \quad (7)$$

where r_i and r_j are the radii of the two contact particles. The particle properties were assigned as $G_g = 18$ GPa and $\upsilon_g = 0.15$, in line with Zhou et al. (2026a). The particle density was set to 2500 kg/m^3. To examine the influence of particle morphology, three particle types were employed: spherical particles and two types of non-spherical particles, denoted as clump1 and clump2. The sphere and clump1 particles have a mean particle diameter (D_{50}) of 0.195 mm and a uniformity coefficient (C_u) of 1.25, whereas the clump2 particles possess a D_{50} of 0.216 mm with $C_u = 1.43$. These size distributions were consistent with Zhou et al. (2026b). The adopted particle shapes and particle size distribution are shown in Fig. 1. Table 1 lists the basic parameters used in the DEM simulations.

To introduce different inherent anisotropies, the three assemblies were generated using different preparation routes. Sphere specimens were produced by the radius expansion method (Zhou et al., 2026a), clump1 specimens by the two-stage isotropic consolidation method (Zhao and Guo, 2015) and clump2 specimens by the multi-layer rotational replication method (Zhou et al., 2026b, 2026c). The numbers of particles in the sphere, clump1 and clump2 assemblies were 53,004, 53,004 and 69,531, respectively. After isotropic consolidation to 100 kPa, the void ratios of the sphere, clump1 and clump2 assemblies were 0.584, 0.445 and 0.636, respectively. Further details of the preparation procedures are available in Zhou et al. (2026b). The prepared samples are illustrated in Fig. 2. In all cases, the specimen size exceeded five times the maximum particle diameter, thereby limiting boundary effects and stress heterogeneity (Jamiolkowski et al., 2004). The clump1 and clump2 specimens exhibited inherent cross-anisotropy under an isotropic stress state, with nearly identical responses in the two horizontal directions but a distinct response in the vertical direction. Specifically, clump1 was vertically stiffer, whereas clump2 was horizontally stiffer. These anisotropies arise from the combined effects of particle morphology, specimen preparation method and the associated particle arrangement.

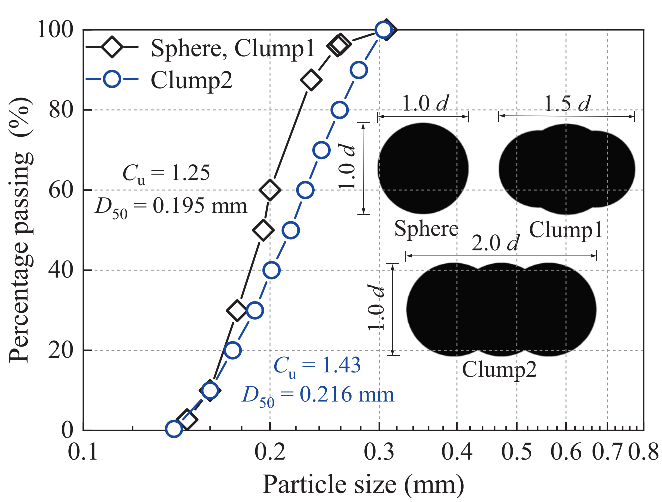

Fig. 1. Particle shape and particle size distribution.

Table 1
Parameters used in the DEM simulations.

Parameters	Value
Particle-particle contact model	Hertz-Mindlin model
Particle density	2500 kg/m^3
Particle shear modulus G_g	18 GPa
Particle Poisson's ratio υ_g	0.15
Interparticle friction coefficient μ	Probe tests: 1.0×10^{23} Consolidation: 0.5
Intermediate principal stress coefficient b	0, 0.25, 0.5, 0.75, 1.0

2.2. True triaxial stress states and probe tests

After consolidation to 100 kPa, the specimens were brought to a range of true triaxial stress states to introduce stress-induced anisotropy. The relationship among the three principal stresses was characterized by the intermediate principal stress coefficient b, defined as:

$$b = \frac{\sigma_x - \sigma_y}{\sigma_z - \sigma_y} \quad (8)$$

where σ_z, σ_x and σ_y denote the effective stresses along z, x and y axes, respectively. b was assigned values of 0, 0.25, 0.5, 0.75 and 1.0. True triaxial loading was carried out under a constant mean effective stress p = 100 kPa. The specimen was compressed or extended along the z direction by varying σ_z from 60 to 140 kPa, while σ_x and σ_y were adjusted by a servo-control mechanism to maintain the prescribed b value (Liu and Yan, 2025):

$$\begin{cases} \sigma_x = \dfrac{(2b-1)\sigma_z + 3p(1-b)}{2-b} \\ \sigma_y = \dfrac{3p-(b+1)\sigma_z}{2-b} \end{cases} \quad (9)$$

The void ratios remained approximately constant after consolidation to the prescribed true triaxial stress states, with only negligible variations. Therefore, no void-ratio normalization was applied to the Young's moduli reported hereafter. These stress states provide a suitable basis for elucidating the combined effects of inherent anisotropy and stress-induced anisotropy on elasticity. At each stress state, directional probe tests were conducted along the z, x and y axes. To obtain the elastic response, the interparticle friction coefficient μ was temporarily assigned a sufficiently large value to prevent contact sliding during probing (Cundall et al., 1989). Taking the z direction as an example, a small stress increment was applied to σ_z, while σ_x and σ_y were kept constant, until the shear strain γ reached 10^{-6} (Zhou et al., 2026c). The Young's modulus, Poisson's ratio and shear strain are defined as:

$$E_i = \frac{\Delta\sigma_i}{\Delta\varepsilon_i} \quad (10)$$

$$\nu_{ij} = -\frac{\Delta\varepsilon_j}{\Delta\varepsilon_i} \quad (11)$$

$$\gamma = \sqrt{\frac{(\Delta\varepsilon_z - \Delta\varepsilon_x)^2 + (\Delta\varepsilon_x - \Delta\varepsilon_y)^2 + (\Delta\varepsilon_y - \Delta\varepsilon_z)^2}{2}} \quad (12)$$

where $\Delta\sigma$ and $\Delta\varepsilon$ are the stress and strain increments induced by the probe test, respectively, with the subscripts denoting the corresponding directions. For ν_{ij}, i and j denote the loading and lateral directions, respectively.

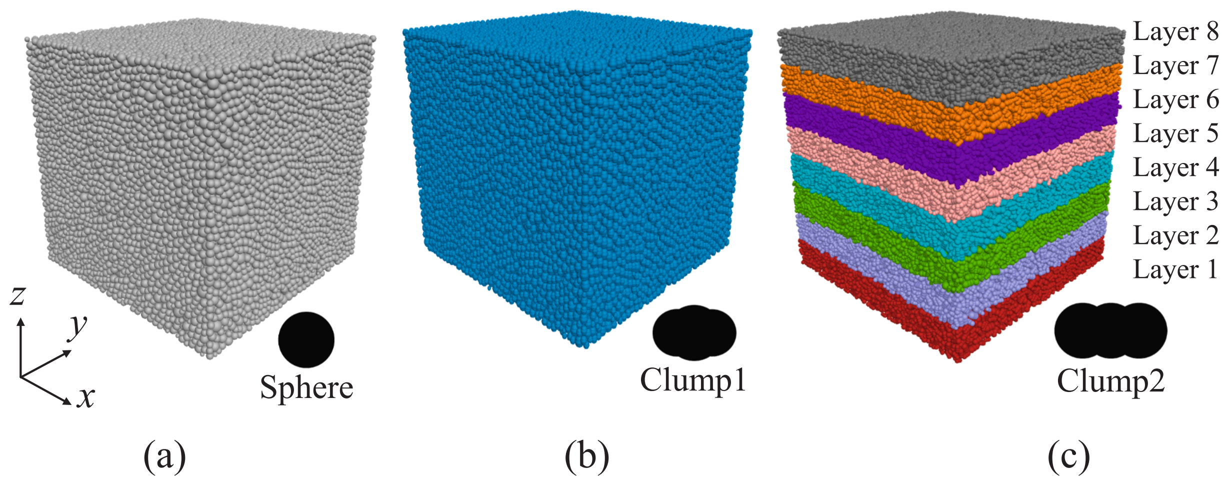

Fig. 2. Sample generation: (a) sphere (radius expansion method); (b) clump1 (two-stage isotropic consolidation method); (c) clump2 (multi-layer rotational replication method), modified from Zhou et al. (2026b).

3. DEM simulation results

3.1. Young's modulus and Poisson's ratio

Fig. 3 shows the evolution of the directional Young's moduli E_i with the corresponding effective stress σ_i under various true triaxial stress states. For the sphere assembly, the three directional moduli follow nearly the same trend and increase with stress, consistent with the stress-dependent form of Eq. (1). The overlapping trends indicate a direction-independent elastic response for the sphere assembly. This is also reflected in Fig. 4a, where the ratios of directional Young's moduli follow a clear power-law relationship with the stress ratios. According to Eq. (1), the modulus ratio can be expressed as $E_i/E_j = (A_i/A_j)(\sigma_i^{m_i}/\sigma_j^{m_j})$. For the sphere assembly, A_i and m_i can be regarded as nearly identical in the three principal directions. The modulus ratio reduces to $E_i/E_j = (\sigma_i/\sigma_j)^m$.

By contrast, clear directional dependence is observed in both clump assemblies. In the clump1 assembly, E_x and E_y nearly coincide, indicating that the elastic characteristics in the horizontal plane are nearly identical, whereas E_z is higher. The clump2 assembly exhibits the opposite pattern: E_x and E_y are broadly comparable, but E_z remains lower than both. These results demonstrate the distinct inherent anisotropies of the two clump assemblies. As shown in Fig. 4b and 4c, the horizontal modulus ratio E_x/E_y can be reasonably described by a power-law relation with σ_x/σ_y, because the two horizontal directions are approximately equivalent. However, the ratios involving the vertical direction, such as E_z/E_x and E_z/E_y, deviate from this simple relation owing to differences in A_i and m_i between the horizontal and vertical directions. This indicates that the anisotropic elasticity of non-spherical assemblies cannot be interpreted solely in terms of stress ratios, but is governed by the combined effects of stress-induced anisotropy and inherent anisotropy. Several data points in Fig. 3b show abrupt reductions in modulus and correspond to the highlighted points in Fig. 4b. As discussed later, these deviations are associated with decreases in the mechanical coordination number (Z_{m}).

The Poisson's ratios are also examined to characterize the lateral strain response under different loading directions. The six Poisson's ratios here are ν_{zx}, ν_{zy}, ν_{xy}, ν_{xz}, ν_{yx} and ν_{yz}. To distinguish different true triaxial stress states, the sign of the deviatoric stress q is taken to be consistent with that of σ_z-σ_y. Accordingly, q is defined as:

$$q = \begin{cases} \sqrt{\dfrac{(\sigma_z-\sigma_x)^2+(\sigma_x-\sigma_y)^2+(\sigma_y-\sigma_z)^2}{2}}, \sigma_z \geqslant \sigma_y \\ -\sqrt{\dfrac{(\sigma_z-\sigma_x)^2+(\sigma_x-\sigma_y)^2+(\sigma_y-\sigma_z)^2}{2}}, \sigma_z < \sigma_y \end{cases} \tag{13}$$

Fig. 5 presents the variations of the Poisson's ratios with q for the sphere assembly under different values of b. These trends can be interpreted with reference to the stress ratios shown in Fig. 6. In general, for loading

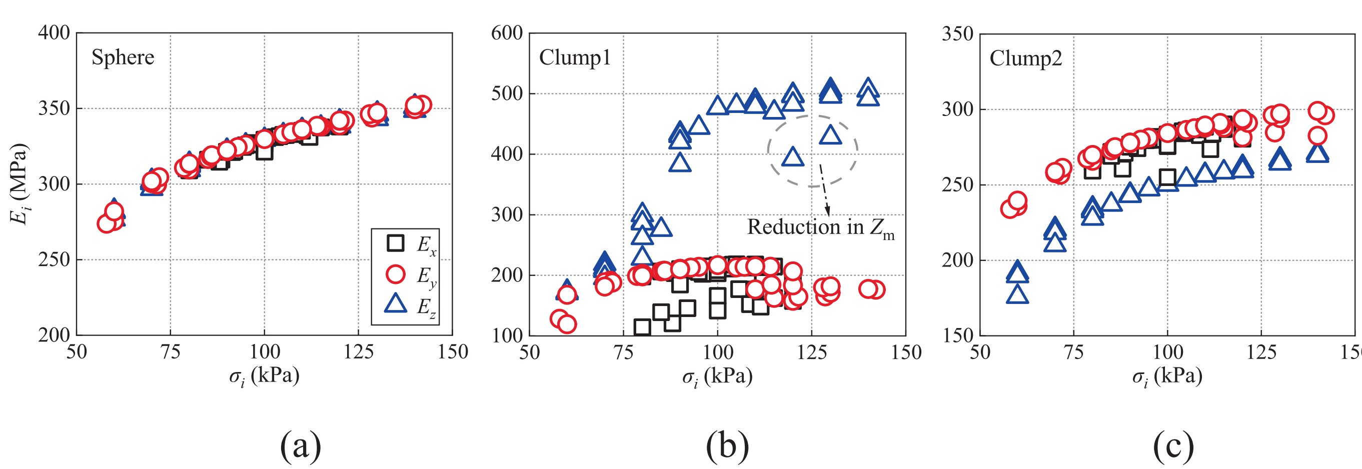

Fig. 3. Variations of Young's moduli with effective stress: (a) sphere assembly; (b) clump1 assembly; (c) clump2 assembly.

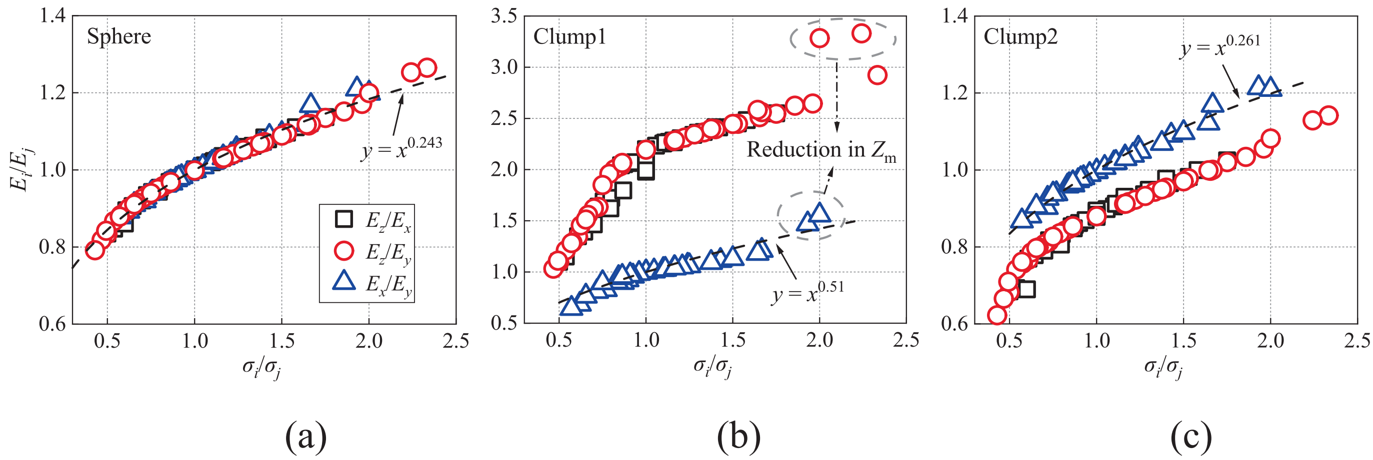

Fig. 4. Relationships between Young's modulus ratios and corresponding stress ratios: (a) sphere assembly; (b) clump1 assembly; (c) clump2 assembly.

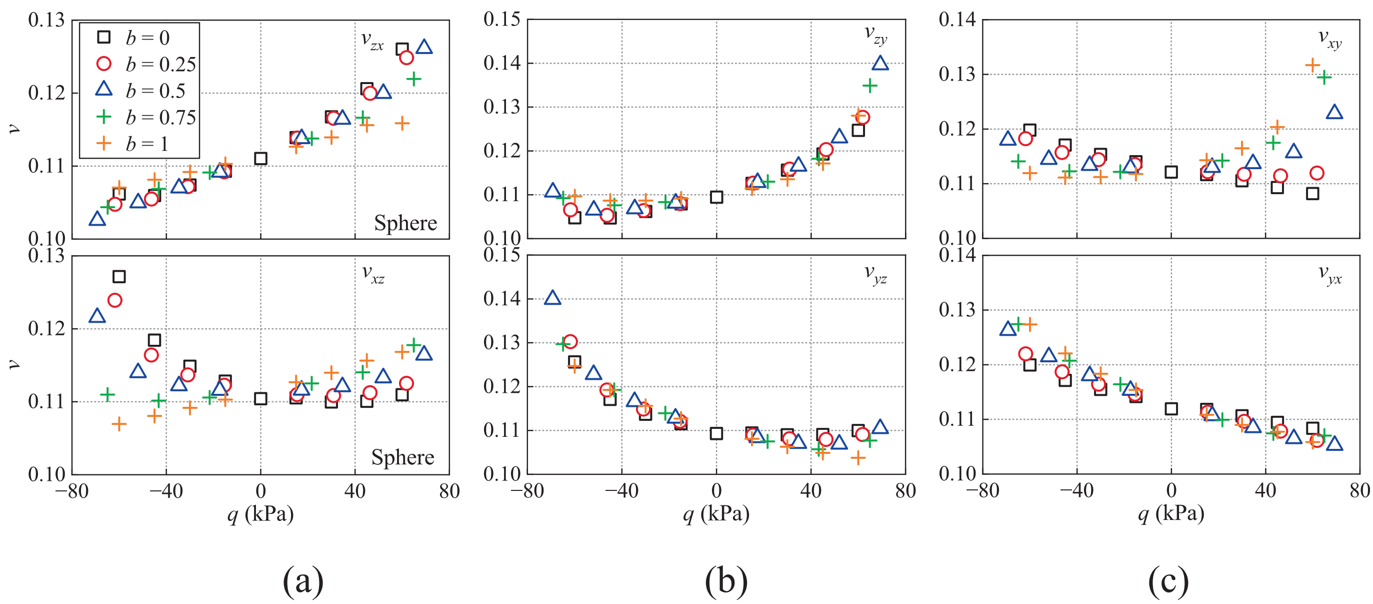

Fig. 5. Variations of Poisson's ratios with deviatoric stress for sphere assembly: (a) ν_{zx} and ν_{xz}; (b) ν_{zy} and ν_{yz}; (c) ν_{xy} and ν_{yx}.

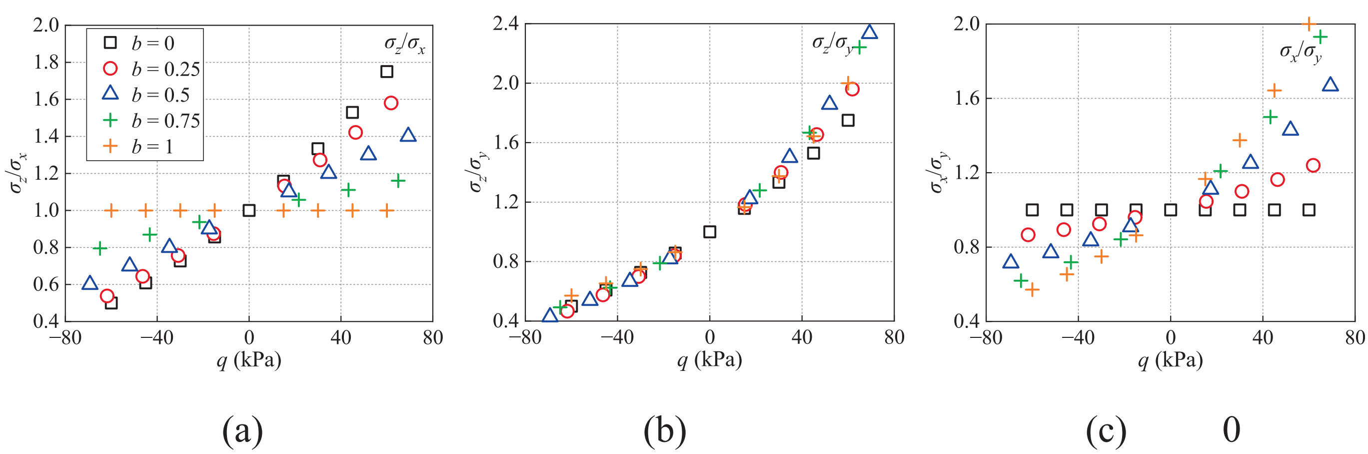

Fig. 6. Variations of stress ratios with deviatoric stress: (a) σ_z/σ_x; (b) σ_z/σ_y; (c) σ_x/σ_y.

along direction i, a lower stress level in the lateral direction j implies weaker lateral constraint and hence a larger ν_{ij}, whereas a higher lateral stress leads to a smaller ν_{ij}. The evolution of the Poisson's ratios is therefore consistent with that of the corresponding stress ratios. For example, the variation of σ_z/σ_x in Fig. 6a explains the behavior of ν_{zx} and ν_{xz}. When $q > 0$, σ_z/σ_x is largest at $b = 0$ and decreases as b approaches 1.0, indicating that the x direction becomes increasingly constrained relative to the z direction. Accordingly, ν_{zx} is larger at lower b, whereas ν_{xz} exhibits the opposite tendency. Similarly, the evolution of σ_z/σ_y in Fig. 6b is consistent with the trends of ν_{zy} and ν_{yz}, while the variation of σ_x/σ_y in Fig. 6c explains the behavior of ν_{xy} and ν_{yx}. The correspondence between Poisson's ratios and stress ratios indicates that, for the sphere assembly, the anisotropy of Poisson's ratios is mainly induced by the relative magnitudes of the stresses.

Fig. 7 shows the variations of Poisson's ratios for the clump1 and clump2 assemblies. Compared with the sphere assembly, the responses of the two clump assemblies are less directly correlated with the stress ratios. This suggests that, for non-spherical assemblies, the evolution of Poisson's ratios is affected not only by the applied stress state but also by the inherent anisotropy introduced during specimen preparation. These observations motivate the theoretical method developed later, in which the directional Young's moduli and Poisson's ratios under true triaxial stress states are predicted through a combination of the hyperelastic model and micromechanically informed tensors.

3.2. Mechanical coordination number and fabric tensors

This section examines the mechanical coordination number (Z_m) and two conventional fabric tensors. Z_m was proposed by Thornton (2000) to quantify the average number of contacts per mechanically active particle. It is defined as:

$$Z_m = \frac{2N_c - N_p^1}{N_p - N_p^0 - N_p^1} \tag{14}$$

where N_c is the total number of interparticle contacts, N_p is the total number of particles, N_p^1 and N_p^0 are the number of particles with only one contact and no contact, respectively.

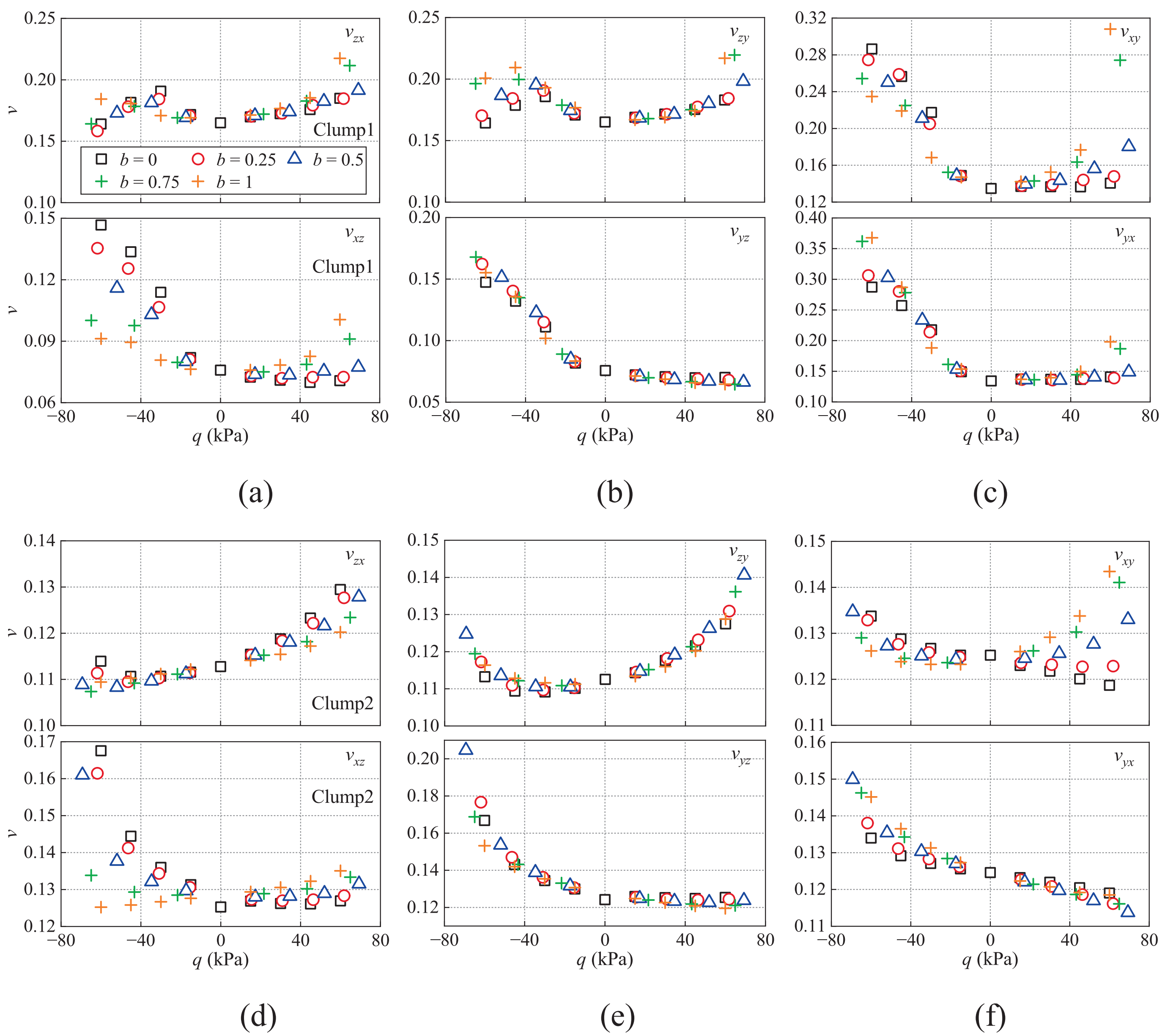

Fig. 7. Variations of Poisson's ratios with deviatoric stress for clump assemblies: (a)-(c) clump1; (d)-(f) clump2.

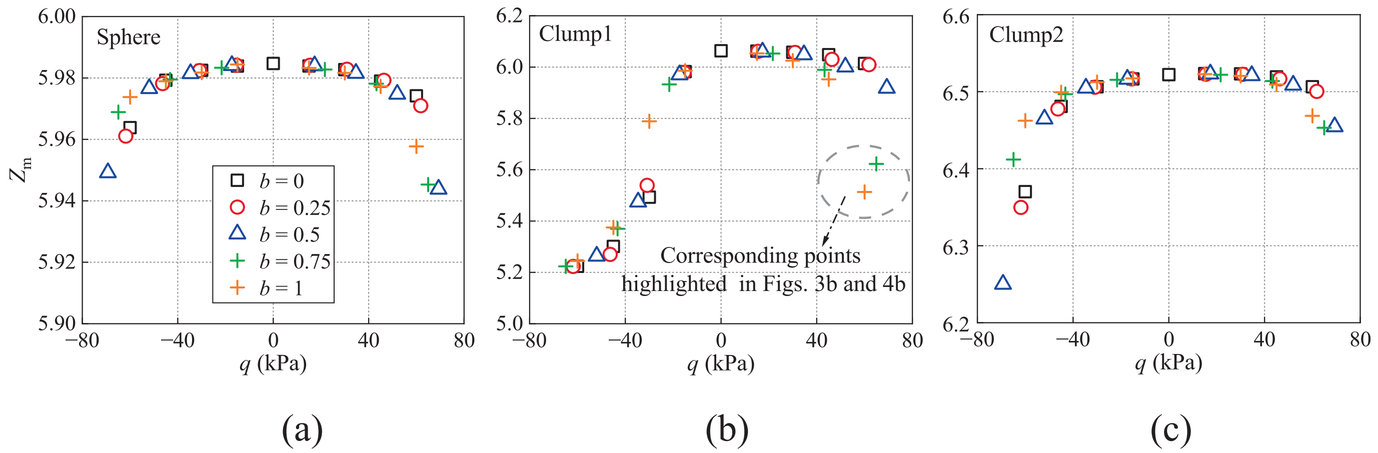

Fig. 8. Variation of mechanical coordination number with deviatoric stress: (a) sphere assembly; (b) clump1 assembly; (c) clump2 assembly.

Fig. 8 shows the variation of Z_m with the deviatoric stress q for the three assemblies. For all particle morphologies, Z_m tends to decrease as q approaches large positive or negative values, indicating a gradual weakening of the load-bearing contact network with increasing stress anisotropy. For the sphere assembly, the variation of Z_m is relatively small, remaining within a narrow range around 5.94–5.99. The responses at positive and negative q are similar, which is consistent with the isotropic geometry of the spherical packing. By contrast, the two clump assemblies exhibit larger variations in Z_m. In both clump1 and clump2, Z_m decreases more rapidly at negative q (i.e., $\sigma_z < \sigma_y$) than at positive q, suggesting a more pronounced loss of load-bearing contacts under this loading direction.

The marked reductions in Z_m observed at some stress states are consistent with the abrupt drops in Young's modulus shown in Fig. 3, confirming the important role of Z_m in controlling the magnitude of elastic stiffness. In particular, the two low values highlighted in Fig. 8b correspond to the highlighted points in Fig. 3b and 4b. However, Z_m is a scalar descriptor and therefore cannot capture the directional differences in elastic response. These differences may instead be associated with the anisotropic organization of the contact network, which is examined next through fabric tensors.

Following Satake (1982) and Gu et al. (2014), the contact normal fabric tensor R_{ij} is defined as:

$$R_{ij} = \frac{1}{N_c}\sum_{N_c} n_i n_j \tag{15}$$

where $\mathbf{n}$ is the unit contact normal vector.

To capture the influence of particle shape, the branch vector fabric H_{ij} is considered. It is calculated as (Kuhn et al., 2015):

$$H_{ij} = \frac{1}{N_c}\sum_{N_c} L_i L_j \tag{16}$$

where $\mathbf{L}$ is the branch vector that connects the centers of contacting particles.

Fig. 9 presents the variation of the contact normal fabric with the effective stress. For the sphere assembly, the three principal components remain close to 1/3, which is the initial isotropic value, and show only minor changes under the prescribed stress states. However, clear inherent anisotropy is observed in the two clump assemblies. For clump1, R_{zz} is lower than R_{xx} and R_{yy}, while the latter two are nearly identical. This indicates that the contact normal distribution is almost the same in the two horizontal directions, but differs clearly in the vertical direction. Clump2 exhibits the opposite pattern, with R_{zz} larger than R_{xx} and R_{yy}. These contrasting trends confirm that the two clump assemblies possess different inherent anisotropies. Meanwhile, the gradual evolution of the fabric components with stress also reflects the development of stress-induced anisotropy.

The branch vector fabric is shown in Fig. 10. For the sphere assembly, the three components of H_{ij} are almost identical and vary slightly with stress. For clump1, H_{zz} is larger than H_{xx} and H_{yy}, whereas the latter two are almost the same. The opposite trend is observed in clump2. It is noted that the branch vector fabric exhibits a trend generally opposite to that of the contact normal fabric. For example, in clump1, R_{zz} is lower than R_{xx} and R_{yy}, whereas H_{zz} is higher than H_{xx} and H_{yy}. This contrast

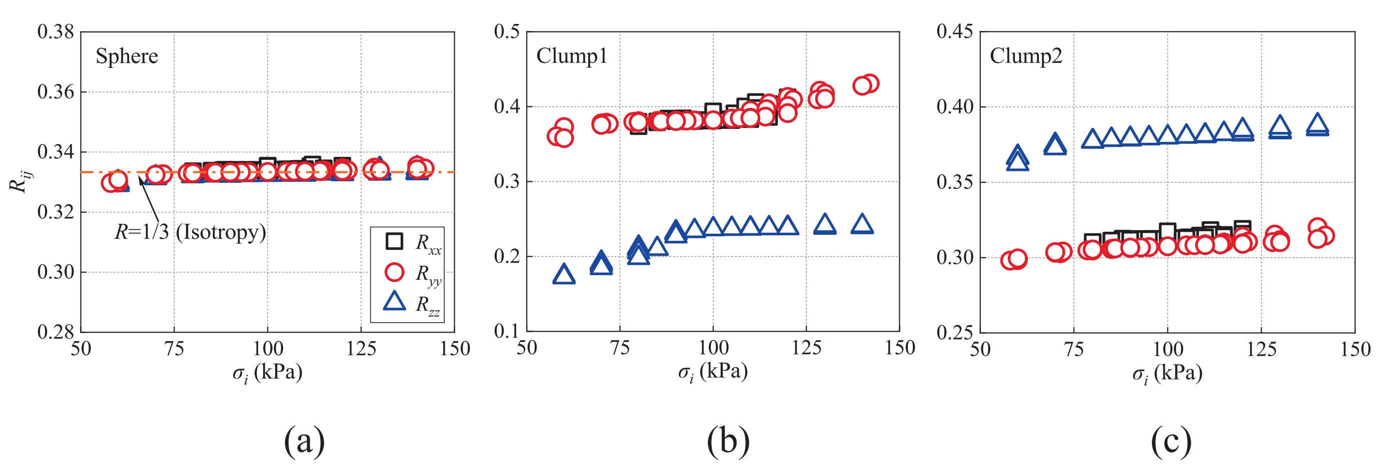

Fig. 9. Variation of contact normal fabric R_{ij} with effective stress: (a) sphere assembly; (b) clump1 assembly; (c) clump2 assembly.

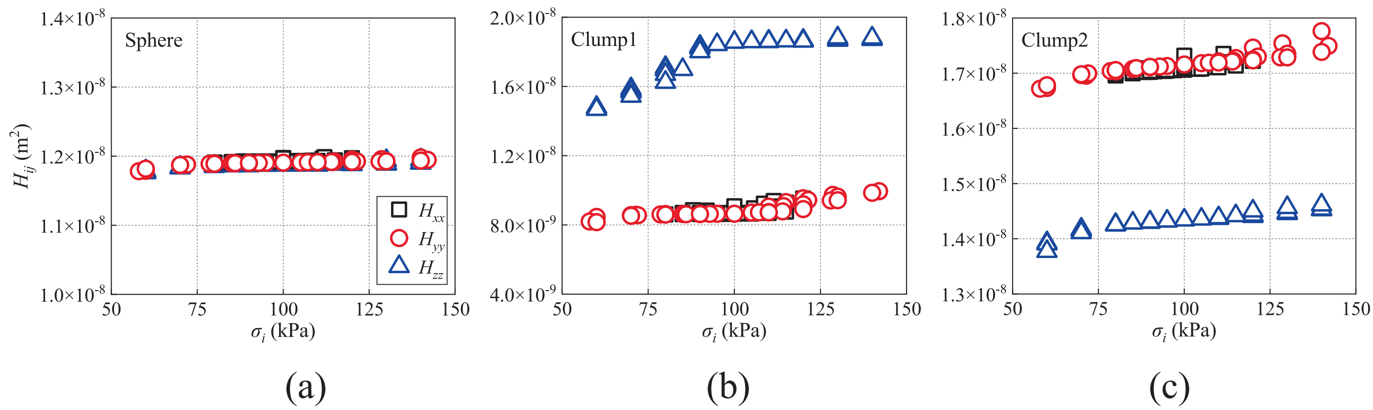

Fig. 10. Variation of branch vector fabric H_{ij} with effective stress: (a) sphere assembly; (b) clump1 assembly; (c) clump2 assembly.

arises because H_{ij} reflects not only directional information but also branch length effects. Taken together, the contact normal fabric and branch vector fabric provide a preliminary description of the specimen microstructure. Nevertheless, they are insufficient to explain the anisotropic elasticity reported in Section 3.1. A more targeted micromechanical description is therefore needed, as developed in the following section.

4. Theoretical methods

4.1. Hyperelastic model

An orthotropic hyperelastic formulation is introduced to describe the anisotropic elasticity. Hyperelastic formulations have been widely adopted to represent the elastic response of granular materials (Houlsby et al., 2019; Amorosi et al., 2020, 2021; Singh and Buscarnera, 2025; Zhou et al., 2026b), because they allow the stress–strain relationship to be derived from thermodynamic principles. Within the elastic range, the soil is assumed to behave as a linear elastic material. The Helmholtz free-energy potential can then be written as follows (Houlsby et al., 2019; Singh and Buscarnera, 2025):

$$\psi = \frac{K}{2}\mathrm{tr}^2(\bar{\varepsilon}) + G\mathrm{tr}\left(\bar{\varepsilon}^{'\mathrm{sym}^2}\right) = \frac{K}{2}\bar{\varepsilon}_{ii}\bar{\varepsilon}_{jj} + G\bar{\varepsilon}_{ij}^{'\mathrm{sym}}\bar{\varepsilon}_{ji}^{'\mathrm{sym}} \tag{17}$$

where K and G denote the elastic bulk and shear moduli in the hyperelastic model, respectively. $\bar{\varepsilon}$ is an equivalent strain tensor, defined as $\bar{\varepsilon} = \mathbf{a}\varepsilon\mathbf{a}^{\mathrm{T}}$, in which $\mathbf{a}$ is an elastic fabric tensor that describes the directional dependence of the elasticity. Here, $\bar{\varepsilon}'$ is the deviatoric part of $\bar{\varepsilon}$. $\bar{\varepsilon}^{\mathrm{sym}}$ denotes the symmetric part of $\bar{\varepsilon}$, given by $\bar{\varepsilon}^{\mathrm{sym}} = (\bar{\varepsilon} + \bar{\varepsilon}^{\mathrm{T}})/2$. Differentiation of Eq. (17) yields the corresponding stiffness tensor as:

$$\begin{aligned} D_{ijkl} &= \frac{\partial \sigma_{ij}}{\partial \varepsilon_{kl}} = \frac{\partial}{\partial \varepsilon_{kl}}\left(\frac{\partial \psi}{\partial \varepsilon_{ij}}\right) = \frac{\partial \bar{\varepsilon}_{mn}}{\partial \varepsilon_{ij}}\frac{\partial^2 \psi}{\partial \bar{\varepsilon}_{mn}\partial \bar{\varepsilon}_{pq}}\frac{\partial \bar{\varepsilon}_{pq}}{\partial \varepsilon_{kl}} \\ &= a_{mi}a_{nj}(K\delta_{mn}\delta_{pq} + 2GP^{\mathrm{sym}}_{mnpq})a_{pk}a_{ql} \end{aligned} \tag{18}$$

where

$$P^{\mathrm{sym}}_{ijkl} = \frac{1}{2}(\delta_{ik}\delta_{jl} + \delta_{il}\delta_{jk}) - \frac{1}{3}\delta_{ij}\delta_{kl} \tag{19}$$

To simplify the formulation, the elastic fabric tensor $\mathbf{a}$ is assumed to be coaxial with the stress reference system (Amorosi et al., 2020; Singh and Buscarnera, 2025). Accordingly, $\mathbf{a}$ reduces to a diagonal form and Eq. (18) can be expressed as follows (Zhou et al., 2026b):

$$\begin{bmatrix} \Delta\sigma_1 \\ \Delta\sigma_2 \\ \Delta\sigma_3 \end{bmatrix} = \begin{bmatrix} D_{11}a_1^4 & D_{12}a_1^2a_2^2 & D_{13}a_1^2a_3^2 \\ D_{12}a_2^2a_1^2 & D_{22}a_2^4 & D_{23}a_2^2a_3^2 \\ D_{13}a_3^2a_1^2 & D_{23}a_3^2a_2^2 & D_{33}a_3^4 \end{bmatrix} \begin{bmatrix} \Delta\varepsilon_1 \\ \Delta\varepsilon_2 \\ \Delta\varepsilon_3 \end{bmatrix} \tag{20}$$

where a_1, a_2, a_3 represent the eigenvalues of $\mathbf{a}$, $D_{11} = D_{22} = D_{33} = K+(4G/3)$ and $D_{12} = D_{13} = D_{23} = K\text{-}(2G/3)$. For notational convenience, the subscripts 1, 2 and 3 hereafter denote the x, y and z directions, respectively.

Explicit expressions for the Young's modulus, Poisson's ratio and shear modulus can be derived as follows:

$$E_i = \frac{9KG}{3K+G}a_i^4 \tag{21}$$

$$\nu_{ij} = \frac{3K-2G}{2(3K+G)}\frac{a_i^2}{a_j^2} \tag{22}$$

$$G_{ij} = Ga_i^2a_j^2 \tag{23}$$

Eqs. (21)-(23) provide explicit expressions for the elastic constants of an orthotropic material. Here, K and G are scalar stiffness parameters that govern the magnitude of the elastic constants, whereas the tensor $\mathbf{a}$ characterizes the directional differences. Under cross-anisotropic conditions, the above expressions reduce to:

$$\frac{a_{\mathrm{h}}^2}{a_{\mathrm{v}}^2} = \frac{G_{\mathrm{hh}}}{G_{\mathrm{vh}}} = \sqrt{\frac{E_{\mathrm{h}}}{E_{\mathrm{v}}}} = \frac{\nu_{\mathrm{hh}}}{\nu_{\mathrm{vh}}} \tag{24}$$

where the subscripts v and h indicate the vertical and horizontal directions, respectively. Eq. (24) is consistent with the relation proposed by Graham and Houlsby (1983), indicating that the present formulation encompasses their assumption as a special case. Furthermore, imposing the condition det($\mathbf{a}$) = 1 (Amorosi et al., 2020), one obtains:

$$a_i^2 = \frac{E_i^{1/3}}{(E_jE_k)^{1/6}} \tag{25}$$

Eq. (25) is used to evaluate the elastic fabric tensor $\mathbf{a}$ in this study.

As discussed above, Z_{m} is a scalar parameter closely associated with the magnitude of elastic stiffness. It is reasonable to expect a close correlation between Z_{m} and K and G. Fig. 11 shows the relationships of K and G with Z_{m} for the three assemblies. In all cases, both K and G exhibit clear dependence on Z_{m}. To quantify these relationships, quadratic functions were adopted: K or $G = c_1Z_{\mathrm{m}}^2 + c_2Z_{\mathrm{m}} + c_3$. The fitted curves agree well with the DEM data, with coefficients of determination $R^2 >$ 0.99 in all cases. The fitted coefficients listed in Table 2 differ among the three assemblies, indicating that the specific K-Z_{m} and G-Z_{m} relationships depend on particle morphology and sample preparation method. It is worth noting that previous studies have shown a dependence of Z_{m} on the mean effective stress p (Jiang and Yang, 2024). By implication, K and G may also depend on p. However, since all stress states considered here were maintained at a constant mean effective stress, this effect is not examined in the present study, and K and G are expressed solely as

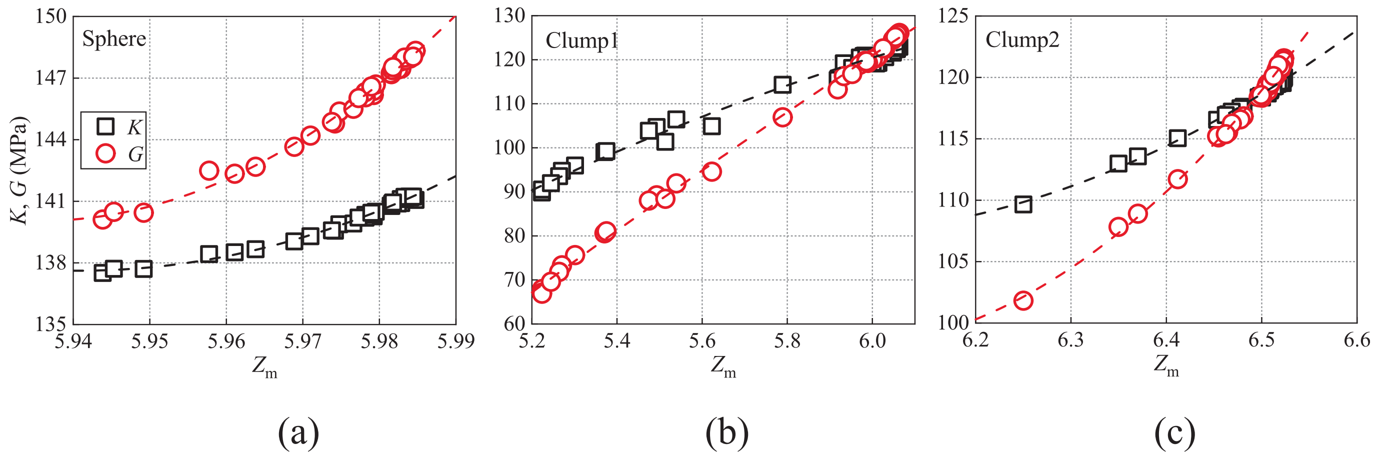

Fig. 11. Relationships between K, G and mechanical coordination number Z_m: (a) sphere assembly; (b) clump1 assembly; (c) clump2 assembly.

Table 2
Coefficients for the relationships between K, G and Z_m.

Assembly	Parameter	c_1	c_2	c_3
Sphere	K	1902.7	−22607.0	67289.1
	G	3386.1	−40197.0	119436.5
Clump1	K	−10.2	151.9	−423.7
	G	−4.7	120.0	−429.6
Clump2	K	48.1	−577.4	1841.7
	G	101.7	−1229.9	3814.8

functions of Z_m.

4.2. Micromechanical method

Having related the scalar stiffness parameters K and G to Z_m, the next step is to evaluate the elastic fabric tensor **a**, which characterizes the directional difference in elastic constants. A micromechanical approach based on the kinematic hypothesis is adopted for this purpose. Following Chang et al. (1995), the stiffness tensor derived from the kinematic hypothesis can be written as:

$$C_{ijkl} = \frac{1}{V}\sum_{N_c} L_i K_{jl} L_k \tag{26}$$

where **L** is the branch vector connecting the centers of contacting particles, V is the specimen volume and **K** is the global contact stiffness, expressed as:

$$K_{ij} = k_n n_i n_j + k_s (s_i s_j + t_i t_j) \tag{27}$$

where **n** is the unit contact normal vector, **s** and **t** are two orthogonal unit vectors lying on the contact plane. The local contact stiffness k_n and k_s are given in Eqs. (5)-(6). The vectors **n**, **s** and **t** are defined as:

$$\mathbf{n} = (\sin\gamma\cos\beta, \sin\gamma\sin\beta, \cos\gamma) \tag{28}$$

$$\mathbf{s} = (\cos\gamma\cos\beta, \cos\gamma\sin\beta, -\sin\gamma) \tag{29}$$

$$\mathbf{t} = (-\sin\beta, \cos\beta, 0) \tag{30}$$

where γ and β are the polar and azimuthal angles of the contact normal, respectively. Since **n**, **s** and **t** form an orthonormal basis:

$$\delta_{ij} = n_i n_j + s_i s_j + t_i t_j \tag{31}$$

Eq. (26) can be rewritten as:

$$C_{ijkl} = \frac{1}{V}\sum_{N_c} k_s L_i L_k \delta_{jl} + \frac{1}{V}\sum_{N_c} (k_n - k_s) L_i L_k n_j n_l \tag{32}$$

Eq. (32) indicates that the stiffness tensor is governed jointly by the interparticle contact stiffness, the branch vector and the contact normal. To incorporate these quantities within the Hertz-Mindlin contact model, two new micromechanical tensors are introduced here: the second-order branch-contact-stiffness fabric tensor **B** and the fourth-order mixed branch-contact-stiffness tensor **M**, defined as follows:

$$B_{ij} = \frac{1}{N_c}\sum_{N_c} \bar{r}^{1/3} N^{1/3} L_i L_j \tag{33}$$

$$M_{ijkl} = \frac{1}{N_c}\sum_{N_c} \bar{r}^{1/3} N^{1/3} L_i n_j L_k n_l \tag{34}$$

where N is the normal contact force and $\bar{r}$ is the effective contact radius. Substituting Eqs. (33)-(34) into Eq. (32) gives:

$$C_{ijkl} = \frac{N_c}{V}\left[C_s B_{ik}\delta_{jl} + (C_n - C_s) M_{ijkl}\right] \tag{35}$$

where C_n and C_s are the coefficients defined in Eqs. (5)-(6). N_c/V is evaluated as (Chang et al., 1995):

$$\frac{N_c}{V} = \frac{3Z_m}{8\pi(1+e)\sum_{N_p} r_i^3} \tag{36}$$

It is important to note that the tangential contribution in Eq. (35) is evaluated using the full tangential contact stiffness. However, previous micromechanical studies have shown that particle rotation may activate zero-energy rotational or shearing mechanisms, so that the tangential resistance is not fully transferred to the macroscopic elastic response (Agnolin and Roux, 2008; Fleischmann et al., 2013b). Fleischmann et al. (2013b) demonstrated that the effect of particle rotation can be represented by replacing the tangential contact stiffness with an effective value, while keeping the normal contact stiffness unchanged. This modification improves the prediction of elastic moduli and Poisson's ratios, consistent with the correction approach adopted by Hicher and Chang (2005). Following this idea, an internal parameter $\zeta \in [0, 1]$ is introduced here to scale the tangential contribution, such that the effective tangential stiffness is defined as $k_s^* = \zeta k_s$ or equivalently $C_s^* = \zeta C_s$. The parameter ζ quantifies the reduction of the effective tangential contact stiffness caused by particle rotation. Accordingly, Eq. (35) is modified as follows:

$$C_{ijkl} = \frac{N_c}{V}\left[C_s^* B_{ik}\delta_{jl} + (C_n - C_s^*)M_{ijkl}\right] \tag{37}$$

Assuming orthotropic symmetry, the elastic stiffness matrix can be written as (Love, 2013):

$$[\boldsymbol{C}] = \begin{bmatrix} C_{11} & C_{12} & C_{13} & 0 & 0 & 0 \\ C_{12} & C_{22} & C_{23} & 0 & 0 & 0 \\ C_{13} & C_{23} & C_{33} & 0 & 0 & 0 \\ 0 & 0 & 0 & C_{44} & 0 & 0 \\ 0 & 0 & 0 & 0 & C_{55} & 0 \\ 0 & 0 & 0 & 0 & 0 & C_{66} \end{bmatrix} \tag{38}$$

The non-zero stiffness components can be obtained in terms of the proposed tensors **B** and **M**. For brevity, the detailed expressions of C_{11}-C_{66} are given in Appendix A. The shear moduli are then obtained as:

$$G_{yz} = C_{44},\ G_{xz} = C_{55},\ G_{xy} = C_{66} \tag{39}$$

The three directional Young's moduli are given by:

$$E_x = \frac{\Delta}{C_{22}C_{33} - C_{23}^2},\ E_y = \frac{\Delta}{C_{11}C_{33} - C_{13}^2},\ E_z = \frac{\Delta}{C_{11}C_{22} - C_{12}^2} \tag{40}$$

where:

$$\Delta = C_{11}C_{22}C_{33} + 2C_{12}C_{13}C_{23} - C_{11}C_{23}^2 - C_{22}C_{13}^2 - C_{33}C_{12}^2 \tag{41}$$

The six directional Poisson's ratios are expressed as:

$$\nu_{xy} = \frac{C_{12}C_{33} - C_{13}C_{23}}{C_{22}C_{33} - C_{23}^2}$$
$$\nu_{xz} = \frac{C_{13}C_{22} - C_{12}C_{23}}{C_{22}C_{33} - C_{23}^2},$$
$$\nu_{yx} = \frac{C_{12}C_{33} - C_{13}C_{23}}{C_{11}C_{33} - C_{13}^2}$$
$$\nu_{yz} = \frac{C_{23}C_{11} - C_{12}C_{13}}{C_{11}C_{33} - C_{13}^2}$$
$$\nu_{zx} = \frac{C_{13}C_{22} - C_{12}C_{23}}{C_{11}C_{22} - C_{12}^2}$$
$$\nu_{zy} = \frac{C_{23}C_{11} - C_{12}C_{23}}{C_{11}C_{22} - C_{12}^2} \tag{42}$$

The above derivations establish a connection between the proposed micromechanical tensors and the directional elastic response under true triaxial stress states. The components of **B** and **M** are not in one-to-one correspondence with the stiffness components C_{ij}, nor do they directly represent the directional Young's moduli. Nevertheless, their evolution provides useful micromechanical insights into the anisotropic elasticity.

The variations of **B** and **M** with effective stress are shown in Fig. 12. For the sphere assembly, the three principal components of **B** collapse onto an almost unique trend and increase with stress, consistent with the nearly coincident directional Young's moduli shown in Fig. 3a. For the clump assemblies, **B** shows clear directional differences. In the clump1 assembly, B_{xx} and B_{yy} show almost the same values, whereas B_{zz} is higher. In the clump2 assembly, the opposite pattern is observed. These trends are qualitatively consistent with those of the Young's moduli in Fig. 3, suggesting that the tensor **B** captures the main directional micromechanical features associated with stiffness anisotropy. The tensor **M** exhibits similar trends, although its relation to the Young's moduli is less direct.

For equal-sized cubic packings of spherical particles under probe test conditions where particle rotation is negligible, $\zeta = 1$. In this special case, the Young's modulus results obtained from Eq. (40) are consistent with the classical micromechanical expressions of Chang et al. (1995) and Yimsiri and Soga (2000), i.e. Eqs. (2)-(4) in this paper. Further verification of the unmodified formulation ($\zeta = 1$) is provided in Appendix B through DEM probe tests at several true triaxial stress states

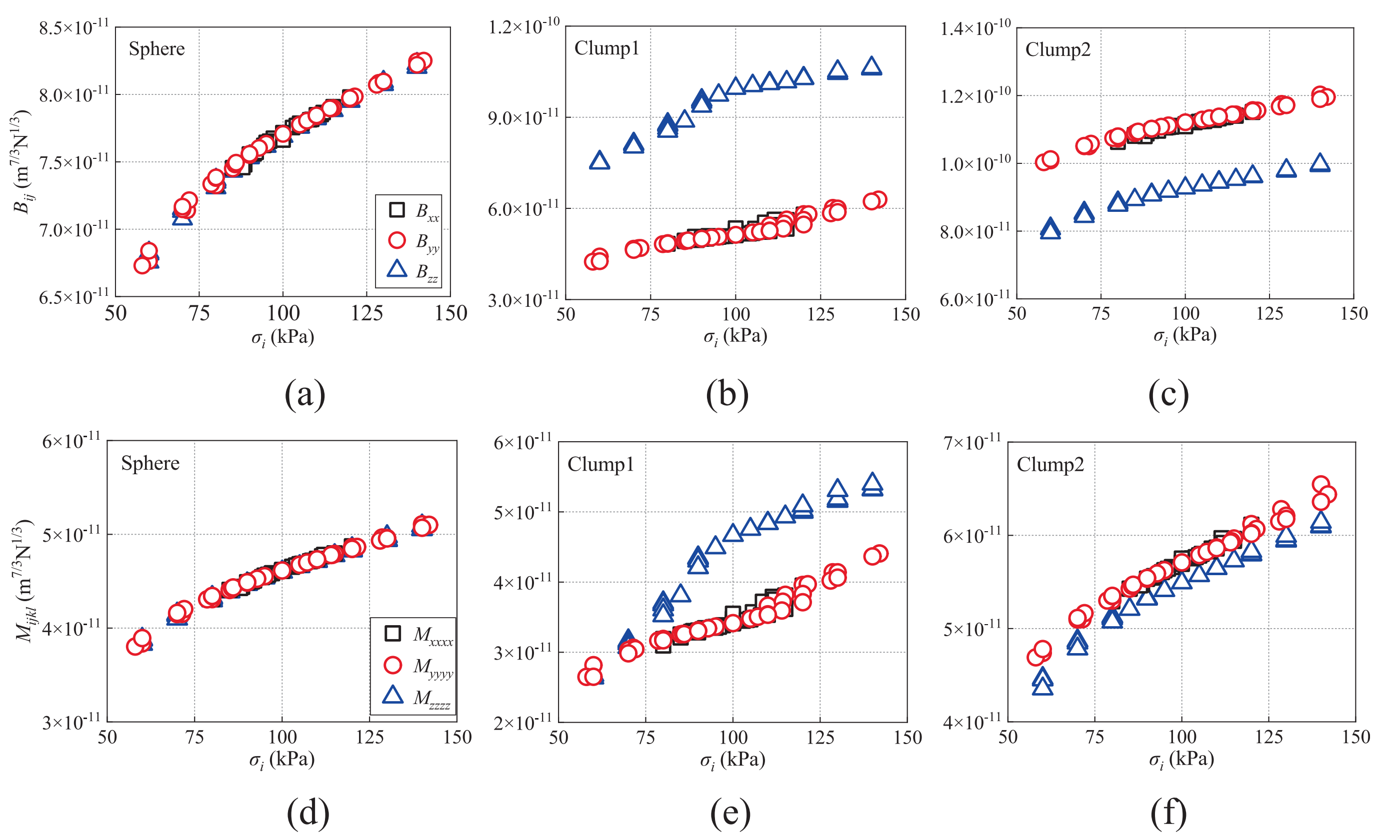

Fig. 12. Variations of the proposed micromechanical tensors with effective stress: B_{ij} for (a) sphere, (b) clump1 and (c) clump2 assemblies; M_{ijkl} for (d) sphere, (e) clump1 and (f) clump2 assemblies.

under conditions where particle rotation is restrained. These comparisons validate the present formulation and its implementation prior to the introduction of the rotation correction factor.

However, particle rotation remains relevant because probe tests are typically designed to suppress interparticle sliding, whereas particle rotation is not constrained (Cundall et al., 1989; Jiang and Yang, 2024; Gong et al., 2024; Chen et al., 2026). In the present study, the effect of particle rotation is incorporated through the correction factor ζ. At the micromechanical level, both the measurement and prediction of particle rotations, as well as their influence on elasticity, remain challenging. As noted by Kruyt et al. (2010), particle rotations are highly sensitive to contact geometry and are therefore difficult to determine accurately. Hence, ζ is determined by calibrating the theoretical predictions against the DEM results. It is assumed that ζ is independent of stress state and depends mainly on particle shape, particle size distribution and initial arrangement. This assumption is supported by the fitted values of ζ, which remain nearly constant across different stress states. Since the specimens exhibit cross-anisotropic characteristics under isotropic consolidation, only two correction factors, ζ_h and ζ_v, are required for the horizontal and vertical directions, respectively.

With these considerations, the above formulations are then used to evaluate the elastic fabric tensor **a** through Eq. (25) and (40). The kinematic hypothesis assumes that all particles deform according to a uniform deformation field and therefore provides an upper-bound solution (Chang et al., 1995). For this reason, the present analysis focuses on the directional contrast of the elastic response, since its magnitude

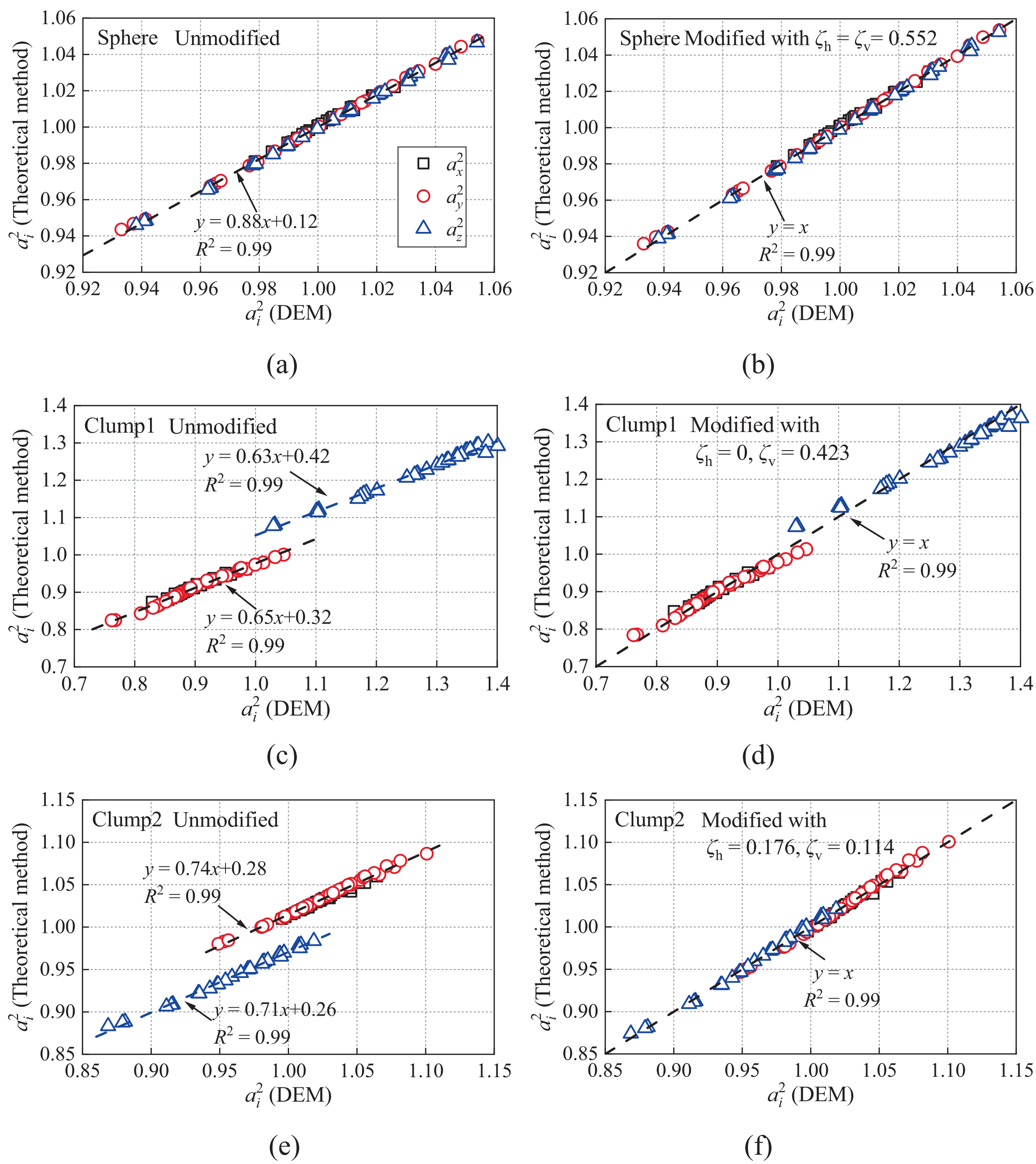

Fig. 13. Comparison between DEM-derived and micromechanically predicted a_i^2 values: (a) sphere, unmodified; (b) sphere, modified; (c) clump1, unmodified; (d) clump1, modified; (e) clump2, unmodified; (f) clump2, modified.

has already been quantitatively linked to Z_m in Section 4.1.

Fig. 13 compares the DEM-derived a_i^2 with the values predicted by the proposed theoretical method. For each particle morphology, the left-hand panel shows the unmodified prediction ($\zeta = 1$), whereas the right-hand panel shows the prediction after applying the correction factors. The horizontal axis represents a_i^2 back-calculated from the Young's moduli in Fig. 3 using Eq. (25), and the vertical axis gives the corresponding values predicted from the proposed micromechanical tensors **B** and **M**.

For the sphere assembly, the unmodified predictions show a strong linear correlation with the DEM results, although the fitted relation deviates from the $y = x$ line. This indicates that the unmodified method can capture the main directional variation of a_i^2, but does not yet provide fully quantitative agreement. After applying $\zeta_h = \zeta_v = 0.552$, the predicted values collapse closely onto the $y = x$ line. This suggests that the tangential contribution is not fully transferred to the macroscopic elastic response even in the sphere assembly. A possible reason is that the specimen is randomly packed and contains a range of particle sizes, allowing particle rotation to develop at contacts and influence the elastic response.

For clump1 and clump2, the unmodified predictions also exhibit clear linear relations with the DEM-derived values. Unlike the sphere assembly, however, these relations cannot be described by a single unified trend before the correction factors are introduced. In both assemblies, the predictions for the horizontal directions, represented by a_x^2 and a_y^2, follow one linear trend, whereas those for the vertical direction follow another. This separation reflects the inherent anisotropy of the specimens and indicates that the contribution of particle rotation differs between the horizontal and vertical directions. After introducing ζ_h and ζ_v, the predicted values in all three directions agree closely with the DEM results, demonstrating that the micromechanical formulation can capture the directional differences in a_i^2 with good accuracy for both spherical and non-spherical assemblies. A further discussion of the linear relations in the unmodified results is provided in Appendix B.

4.3. Validation and discussion

Overall, the results show that the proposed tensors **B** and **M**, together with the correction factor ζ, provide an effective basis for evaluating the elastic fabric tensor **a**. Combined with the K-Z_m and G-Z_m relations established in Section 4.1, the present approach enables the anisotropic elasticity under true triaxial stress states to be described quantitatively. The following comparisons examine the theoretical predictions against the DEM results for both Young's moduli and Poisson's ratios.

Fig. 14 compares the predicted directional Young's moduli with the DEM results. For all three assemblies, the predicted values are in close agreement with the DEM results over a wide range of true triaxial stress states. For the sphere assembly, the three directional moduli are reproduced with very small discrepancies. For the clump1 and clump2 assemblies, the predictions also remain accurate, despite the stronger directional contrast associated with inherent anisotropy.

The comparisons for Poisson's ratios are shown in Fig. 15. The predictions are evaluated using the hyperelastic relation in Eq. (22), rather than the orthotropic compliance expressions in Eq. (42). The proposed method captures the main trends observed in the DEM results, including the variations with stress state and the directional differences among the Poisson's ratio components. The corresponding root mean square error (RMSE) values are 0.003, 0.036 and 0.004 for the sphere, clump1 and clump2 assemblies, respectively. For the sphere assembly, the predicted curves generally follow the DEM results over most stress states. For the two clump assemblies, the main directional patterns are also reproduced, although the agreement is not as close as that for the Young's moduli. This discrepancy is likely related to the directional variation of Poisson's ratios, which does not strictly follow the simple ratio form a_i^2/a_j^2 given by Eq. (22). Similar observations have also been reported in previous DEM studies (Gu et al., 2017; Zhou et al., 2026c).

The above comparisons show that the present method provides an accurate prediction of the directional Young's moduli and a reasonable quantitative description of the Poisson's ratio response under true triaxial stress states. To further examine its generality, an additional validation is performed using an independent DEM dataset reported by Zhou et al. (2026c). In that study, the sphere and clump2 assemblies were generated using the same particle size distributions, particle morphologies and preparation procedures as those adopted in this work. The same correction factors ζ are therefore used. Unlike the true triaxial stress states considered above, the dataset in Zhou et al. (2026c) corresponds to cross-anisotropic stress states, where the horizontal stress σ_h was kept constant at 100 kPa while the vertical stress σ_v was varied. A useful feature of this dataset is that it includes shear moduli in addition to Young's moduli and Poisson's ratios.

Stiffness anisotropy is characterized by the ratios a_h^2/a_v^2, G_{hh}/G_{vh}, $(E_h/E_v)^{0.5}$ and ν_{hh}/ν_{vh}. Fig. 16 compares the predicted a_h^2/a_v^2 obtained from the proposed micromechanical formulation with the corresponding DEM-derived anisotropy measures. The predicted a_h^2/a_v^2 agrees closely with both $(E_h/E_v)^{0.5}$ and G_{hh}/G_{vh} for the sphere and clump2 assemblies. This indicates that the present formulation is able to capture the anisotropy of both Young's modulus and shear modulus. By contrast, ν_{hh}/ν_{vh} follows a visibly different trend, especially at higher stress ratios. This is consistent with the preceding results, which show that the directional variation of Poisson's ratios does not strictly follow the simple anisotropy relation in Eq. (22). The additional comparison provides an independent consistency check and supports the general

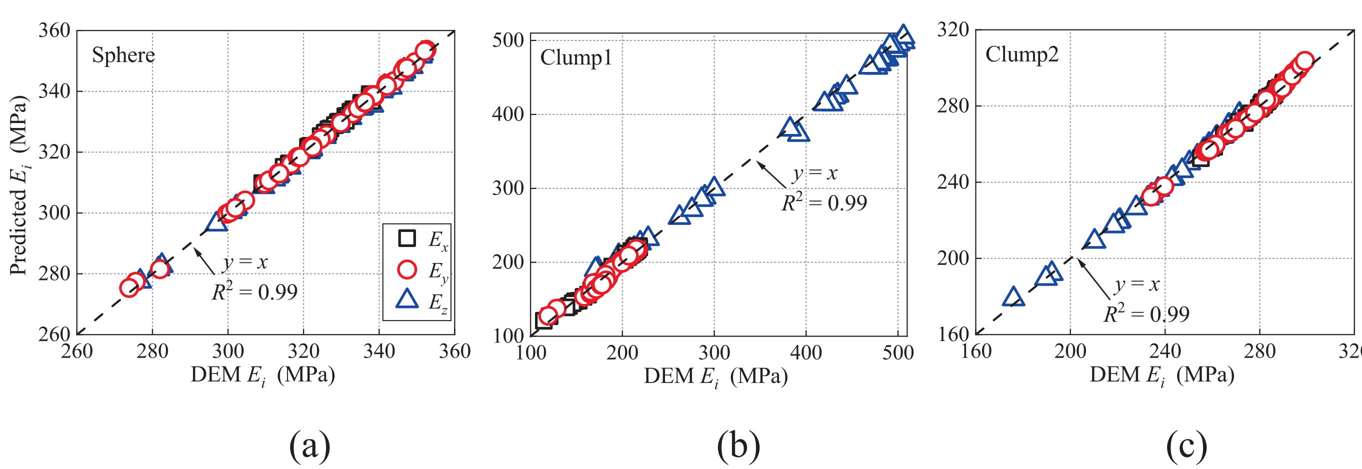

Fig. 14. Comparison between DEM and predicted directional Young's moduli for (a) sphere assembly; (b) clump1 assembly; (c) clump2 assembly.

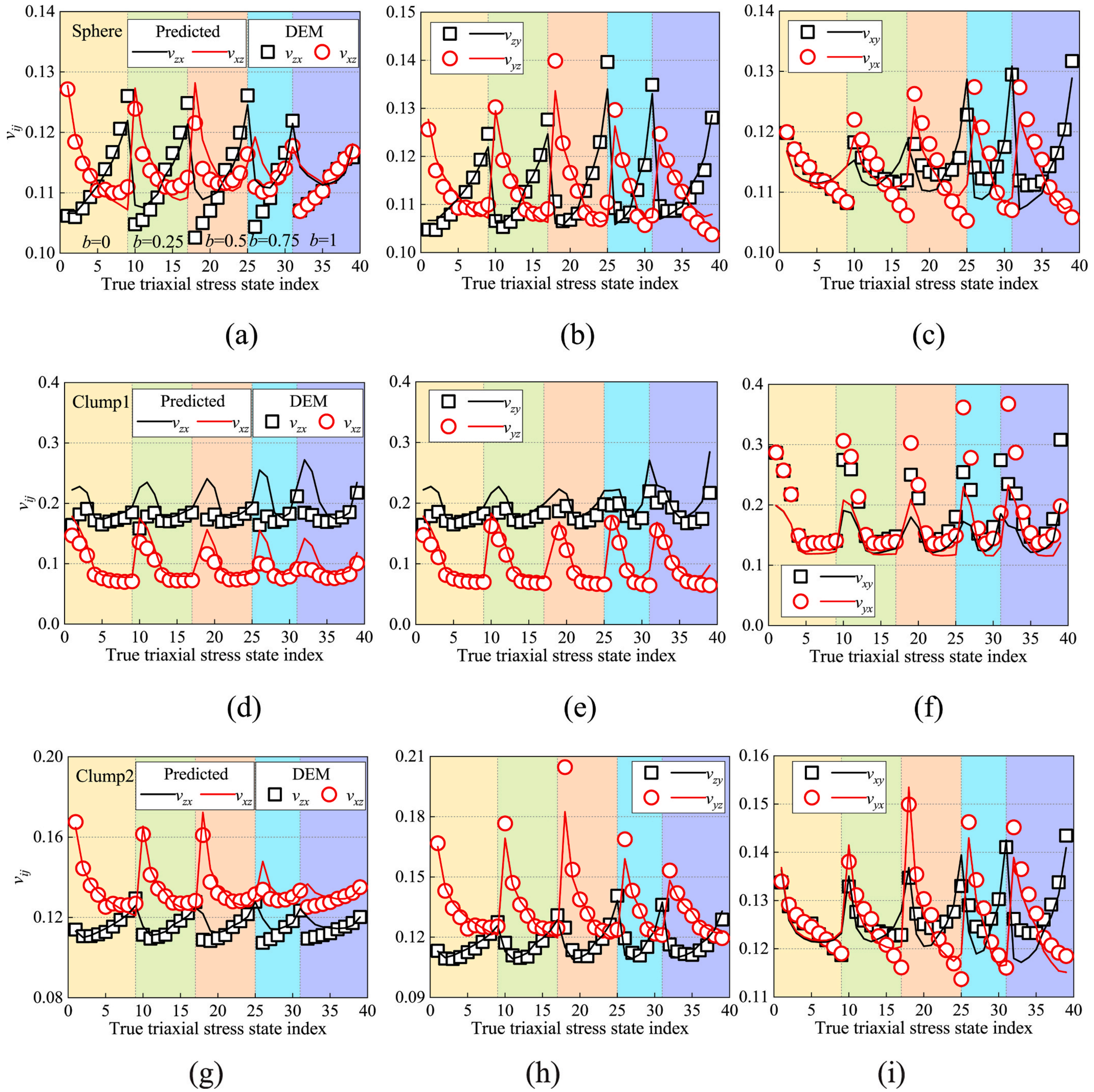

Fig. 15. Comparison between DEM and predicted Poisson's ratios for (a)-(c) sphere assembly, (d)-(f) clump1 assembly and (g)-(i) clump2 assembly: (a), (d) and (g) ν_{zx} and ν_{xz}; (b), (e) and (h) ν_{zy} and ν_{yz}; (c), (f) and (i) ν_{xy} and ν_{yx}. The horizontal axis denotes the true triaxial stress state index, with the corresponding stress states listed in Appendix C.

applicability of the present micromechanical description for quantifying stiffness anisotropy in granular materials.

5. Summary and conclusions

This study uncovered the combined effects of inherent anisotropy and stress-induced anisotropy on the elasticity of granular materials through DEM probe tests on sphere and clump assemblies under a range of true triaxial stress states. A unified description is established in which the directional Young's moduli and Poisson's ratios are interpreted using a hyperelastic formulation, while their directional contrast is characterized through a micromechanical approach. The main conclusions are as follows:

(1) Under true triaxial stress states, both Young's moduli and Poisson's ratios exhibit pronounced directional differences governed by particle morphology and stress state. An orthotropic hyperelastic formulation is developed for granular materials under such conditions. Within this formulation, the scalar stiffness parameters K and G govern the magnitude of the elastic constants, whereas the elastic fabric tensor **a** characterizes the directional differences. Clear quantitative correlations are established between the mechanical coordination number Z_m and K and G.

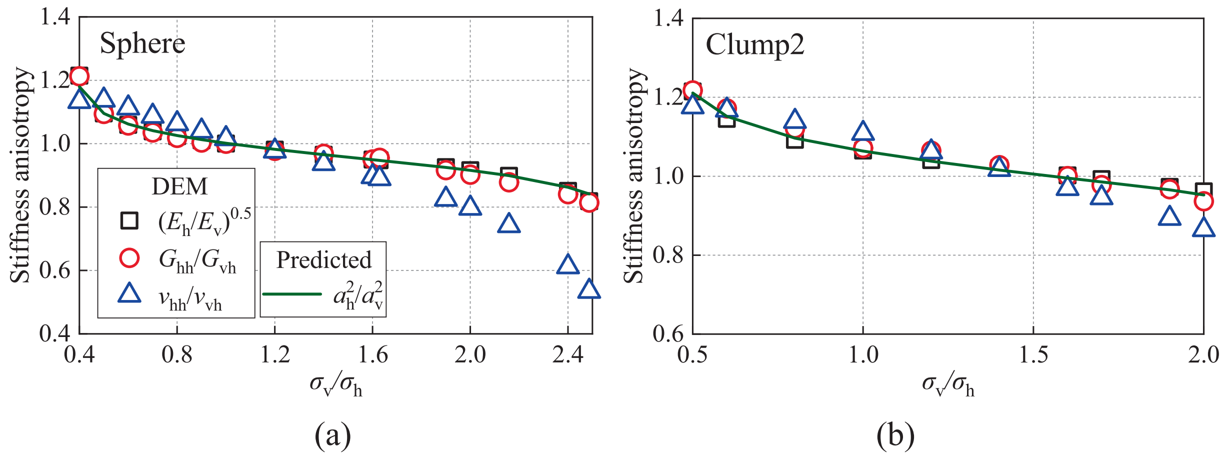

Fig. 16. Comparison between DEM and predicted stiffness anisotropy for (a) sphere assembly; (b) clump2 assembly. DEM data are taken from Zhou et al. (2026c).

(2) Conventional contact normal fabric and branch vector fabric are insufficient to explain the directional elastic response. Based on the kinematic hypothesis, anisotropic elasticity is shown to depend jointly on the interparticle contact stiffness, the branch vector and the contact normal of the granular assemblies. Two new micromechanical tensors, **B** and **M**, are therefore introduced to provide a targeted micromechanical description of directional stiffness anisotropy.

(3) By combining the K-Z_m and G-Z_m relations with the micromechanical formulation, the present approach provides a quantitative description of anisotropic elasticity under true triaxial stress states. The tensors **B** and **M**, together with the particle-rotation correction factor ζ, provide an effective basis for evaluating the elastic fabric tensor **a**. The resulting predictions reproduce the directional Young's moduli accurately and capture the main trends of the Poisson's ratio response. Additional validation against an independent DEM dataset further confirms the generality of the present approach.

CRediT authorship contribution statement

Hechen Zhou: Writing – original draft, Methodology, Investigation, Conceptualization. **Xiaoqiang Gu:** Writing – review & editing, Supervision, Funding acquisition, Conceptualization. **Hai-Lin Wang:** Writing – review & editing, Methodology. **Xiaomin Liang:** Writing – review & editing, Methodology.

Declaration of competing interest

The authors declare that they have no known competing financial interests or personal relationships that could have appeared to influence the work reported in this paper.

Acknowledgements

The work presented in this paper is supported by National Natural Science Foundation of China (Grant No. 52178344 and 42361164615). These supports are gratefully acknowledged.

Appendix A:. Expressions of the orthotropic stiffness components

The expanded expressions of the non-zero stiffness components in Eq. (38) are listed below:

$$C_{11} = C_{1111} = \frac{N_c}{V}\left[C_s^* B_{11} + (C_n - C_s^*)M_{1111}\right] \tag{A1}$$

$$C_{22} = C_{2222} = \frac{N_c}{V}\left[C_s^* B_{22} + (C_n - C_s^*)M_{2222}\right] \tag{A2}$$

$$C_{33} = C_{3333} = \frac{N_c}{V}\left[C_s^* B_{33} + (C_n - C_s^*)M_{3333}\right] \tag{A3}$$

$$C_{12} = \frac{1}{2}(C_{1122} + C_{2211}) = \frac{N_c}{2V}(C_n - C_s^*)(M_{1122} + M_{2211}) \tag{A4}$$

$$C_{13} = \frac{1}{2}(C_{1133} + C_{3311}) = \frac{N_c}{2V}(C_n - C_s^*)(M_{1133} + M_{3311}) \tag{A5}$$

$$C_{23} = \frac{1}{2}(C_{2233} + C_{3322}) = \frac{N_c}{2V}(C_n - C_s^*)(M_{2233} + M_{3322}) \tag{A6}$$

$$C_{44} = \frac{1}{2}(C_{2323} + C_{3232}) = \frac{N_c}{2V}\left[C_s^*(B_{22} + B_{33}) + (C_n - C_s^*)(M_{2323} + M_{3232})\right] \tag{A7}$$

$$C_{55} = \frac{1}{2}(C_{1313} + C_{3131}) = \frac{N_c}{2V}\left[C_s^*(B_{11} + B_{33}) + (C_n - C_s^*)(M_{1313} + M_{3131})\right] \tag{A8}$$

$$C_{66} = \frac{1}{2}(C_{1212} + C_{2121}) = \frac{N_c}{2V}\left[C_s^*(B_{11} + B_{22}) + (C_n - C_s^*)(M_{1212} + M_{2121})\right] \tag{A9}$$

The above expressions are then substituted into Eqs. (39)-(42) to obtain the directional Young's moduli, Poisson's ratios and shear moduli in the main text.

Appendix B:. Verification of the unmodified formulation ($\zeta = 1$)

In Section 4.2, the correction factor ζ is introduced to account for the influence of particle rotation. To examine the performance of the formulation before this correction is applied, DEM probe tests were performed under conditions where particle rotation was restrained. Table B1 compares the DEM-derived directional Young's moduli and anisotropy parameters with the predictions of the unmodified formulation. For all three particle morphologies, the predicted Young's moduli exceed the DEM results, as expected from the upper-bound solution of the kinematic hypothesis (Chang et al., 1995). Nevertheless, the anisotropy parameters a_i^2 agree closely with the DEM values, indicating that the unmodified formulation captures the directional contrast of elasticity accurately when particle rotation is restrained.

Table B1
Comparison of predicted and DEM-derived directional Young's moduli and anisotropy parameters a_i^2 for selected stress states of assemblies.

Assembly	(σ_x, σ_y, σ_z) (kPa)	Predicted E_i (MPa) and a_i^2			DEM E_i (MPa) and a_i^2		
		E_x (a_x^2)	E_y (a_y^2)	E_z (a_z^2)	E_x (a_x^2)	E_y (a_y^2)	E_z (a_z^2)
Sphere*	(100,100,100)	386.7 (1.00)	386.7 (1.00)	386.7 (1.00)	386.1 (1.00)	386.1 (1.00)	386.1 (1.00)
Sphere	(100,100,100)	456.9 (1.00)	456.9 (1.00)	456.9 (1.00)	418.7 (1.00)	418.7 (1.00)	418.7 (1.00)
Sphere	(100,60,140)	455.4 (1.01)	400.8 (0.95)	489.7 (1.05)	415.3 (1.01)	367.2 (0.95)	446.5 (1.05)
Clump1	(100,100,100)	340.5 (0.90)	340.5 (0.90)	648.0 (1.24)	306.0 (0.90)	306.0 (0.90)	581.5 (1.24)
Clump1	(100,60,140)	335.5 (0.91)	287.6 (0.84)	684.7 (1.30)	297.3 (0.91)	255.4 (0.84)	604.2 (1.30)
Clump2	(100,100,100)	490.5 (1.03)	490.5 (1.03)	413.1 (0.94)	405.1 (1.03)	405.1 (1.03)	346.2 (0.95)
Clump2	(100,60,140)	488.5 (1.03)	441.6 (0.98)	442.1 (0.98)	399.9 (1.03)	356.6 (0.97)	371.2 (0.99)

Note: * denotes the equal-sized cubic packing of spherical particles. The DEM results in this table were obtained from probe tests with particle rotation restrained.

The above results confirm the validity of the unmodified formulation when particle rotation is restrained. When particle rotation is allowed, clear trends can still be identified, as discussed below. The results in Fig. 13 show linear relations between the DEM-derived and theoretically obtained a_i^2. The general form of these relations is illustrated in Fig. B1. For the sphere assembly, the isotropic state provides a reference point, where both the DEM-derived and theoretical values satisfy $a_i^2 = 1$. Therefore, the linear relation is constrained to pass through $(1, 1)$. Once the DEM-derived and theoretical values at one anisotropic stress state are available, the slope λ of this relation can be determined. For the clump assemblies, inherent anisotropy exists. The reference point is therefore not $(1, 1)$, but (x_0, y_0), where x_0 denotes the DEM-derived a_z^2 at the isotropically consolidated state and y_0 denotes the corresponding theoretical value of a_z^2. Since $\det(\mathbf{a}) = 1$ and the clump assemblies are cross-anisotropic at the isotropic stress state ($a_x^2 = a_y^2$), the horizontal reference point is given by $(1/(x_0)^{0.5}, 1/(y_0)^{0.5})$. With results from at least one additional anisotropic stress state, the two slopes λ_h and λ_v can be determined. The slopes are expected to depend mainly on particle shape, particle-size distribution and initial arrangement. These relations indicate that the unmodified formulation already captures the main directional tendency of a_i^2, although a systematic bias remains when particle rotation is allowed.

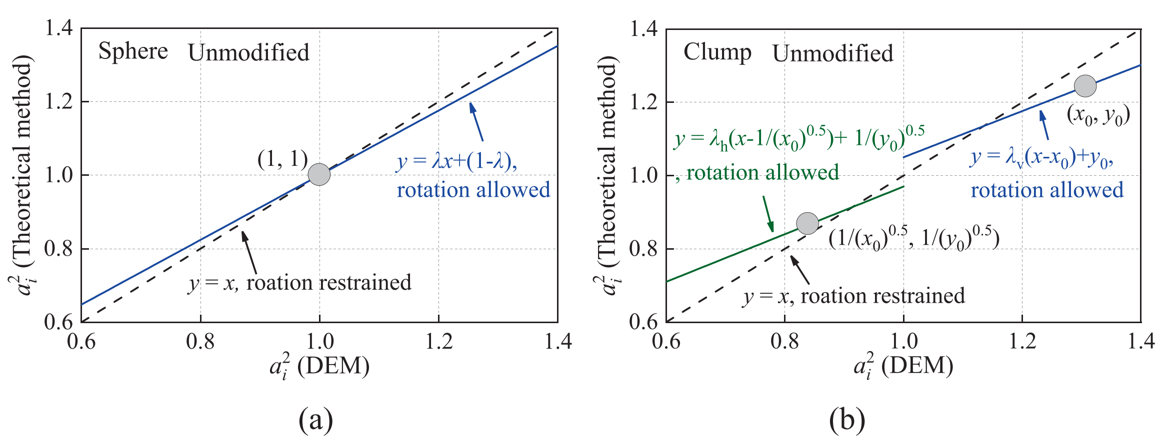

Fig. B1. Schematic illustration of the linear relations in the unmodified results: (a) sphere assembly; (b) clump assembly

Appendix C:. True triaxial stress states

.

Table C1
True triaxial stress states used in the DEM simulation.

ID	σ_x	σ_y	σ_z	q	ID	σ_x	σ_y	σ_z	q	ID	σ_x	σ_y	σ_z	q
1	100	100	100	0	14	102.9	107.1	90	−15.5	27	108	72	120	43.3
2	95	95	110	15	15	105.7	114.3	80	−30.9	28	112	58	130	64.9
3	90	90	120	30	16	108.6	121.4	70	−46.4	29	96	114	90	−21.6
4	85	85	130	45	17	111.4	128.6	60	−61.8	30	92	128	80	−43.3
5	80	80	140	60	18	100	90	110	17.3	31	88	142	70	−64.9
6	105	105	90	−15	19	100	80	120	34.6	32	105	90	105	15
7	110	110	80	−30	20	100	70	130	52.0	33	110	80	110	30
8	115	115	70	−45	21	100	60	140	69.3	34	115	70	115	45
9	120	120	60	−60	22	100	110	90	−17.3	35	120	60	120	60
10	97.1	92.9	110	15.5	23	100	120	80	−34.6	36	95	110	95	−15
11	94.3	85.7	120	30.9	24	100	130	70	−52.0	37	90	120	90	−30
12	91.4	78.6	130	46.4	25	100	140	60	−69.3	38	85	130	85	−45
13	88.6	71.4	140	61.8	26	104	86	110	21.6	39	80	140	80	−60

Note: ID denotes the stress state index used in Fig. 15. All stresses are in kPa.

Data availability

Data will be made available on request.

References

Agnolin, I., Roux, J.N., 2008. On the elastic moduli of three-dimensional assemblies of spheres: Characterization and modeling of fluctuations in the particle displacement and rotation. Int. J. Solids Struct. 45 (3–4), 1101–1123.
Amorosi, A., Rollo, F., Houlsby, G.T., 2020. A nonlinear anisotropic hyperelastic formulation for granular materials: comparison with existing models and validation. Acta Geotech. 15 (1), 179–196.
Amorosi, A., Rollo, F., Dafalias, Y.F., 2021. Relating elastic and plastic fabric anisotropy of clays. Géotechnique 71 (7), 583–593.
Bellotti, R., Jamiolkowski, M., Lo Presti, D.C.F., et al., 1996. Anisotropy of small strain stiffness in Ticino sand. Géotechnique 46 (1), 115–131.
Callisto, L., Rampello, S., 2002. Shear strength and small-strain stiffness of a natural clay under general stress conditions. Géotechnique 52 (8), 547–560.
Castellón, J., Ledesma, A., 2022. Small strains in soil constitutive modeling. Arch. Comput. Meth. Eng. 29, 3223–3280.
Chang, C.S., Chao, S.J., Chang, Y., 1995. Estimates of elastic moduli for granular material with anisotropic random packing structure. Int. J. Solids Struct. 32 (14), 1989–2008.
Chen, T.H., Yang, Z.X., Yu, Y., 2026. An anisotropic elastic model for granular materials derived from stress probing tests. Comput. Geotech. 191, 107818.
Clayton, C.R.I., 2011. Stiffness at small strain: research and practice. Géotechnique 61 (1), 5–37.
Cundall, P.A., Strack, O.D.L., 1979. A discrete numerical model for granular assemblies. Géotechnique 29 (1), 47–65.
Cundall, P.A., Jenkins, J.T., Ishibashi, I., 1989. Evolution of elastic moduli in a deforming granular assembly. In: Biarez, J., Gourves, R. (Eds.), Powders and Grains. Balkema, Rotterdam, pp. 319–322.
Dutta, T.T., Otsubo, M., Kuwano, R., et al., 2020. Estimating multidirectional stiffness of soils using planar piezoelectric transducers in a large triaxial apparatus. Soils Found. 60 (5), 1269–1286.
Ezaoui, A., Di Benedetto, H., 2009. Experimental measurements of the global anisotropic elastic behaviour of dry Hostun sand during triaxial tests, and effect of sample preparation. Géotechnique 59 (7), 621–635.
Fleischmann, J.A., Drugan, W.J., Plesha, M.E., 2013a. Direct micromechanics derivation and DEM confirmation of the elastic moduli of isotropic particulate materials: Part I No particle rotation. J. Mech. Phys. Solids 61 (7), 1569–1584.
Fleischmann, J.A., Drugan, W.J., Plesha, M.E., 2013b. Direct micromechanics derivation and DEM confirmation of the elastic moduli of isotropic particulate materials: Part II Particle rotation. J. Mech. Phys. Solids 61 (7), 1585–1599.
Gasparre, A., Nishimura, S., Minh, N.A., et al., 2007. The stiffness of natural London clay. Géotechnique 57 (1), 33–47.
Gong, J., Pang, X.W., Tang, Y., et al., 2024. Effects of particle shape, physical properties and particle size distribution on the small-strain stiffness of granular materials: a DEM study. Comput. Geotech. 165, 105903.
Graham, J., Houlsby, G.T., 1983. Anisotropic elasticity of a natural clay. Géotechnique 33 (2), 165–180.
Gu, X.Q., Yang, J., Huang, M.S., 2013. DEM simulations of the small strain stiffness of granular soils: effect of stress ratio. Granul. Matter 15 (3), 287–298.
Gu, X.Q., Huang, M.S., Qian, J.G., 2014. DEM investigation on the evolution of microstructure in granular soils under shearing. Granul. Matter 16 (1), 91–106.
Gu, X.Q., Hu, J., Huang, M.S., 2017. Anisotropy of elasticity and fabric of granular soils. Granul. Matter 19 (2), 33.
Gu, X.Q., Liang, X.M., Hu, J., 2024. Quantifying fabric anisotropy of granular materials using wave velocity anisotropy: a numerical investigation. Géotechnique 74 (12), 1263–1275.
Hardin, B.O., Richart, F.E., 1963. Elastic wave velocities in granular soils. J. Soil Mech. Found. Eng. Div. 89 (1), 39–56.
Hicher, P.Y., Chang, C.S., 2005. Evaluation of two homogenization techniques for modeling the elastic behavior of granular materials. J. Eng. Mech. 131 (11), 1184–1194.
Hoque, E., Tatsuoka, F., 2004. Effects of stress ratio on small-strain stiffness during triaxial shearing. Géotechnique 54 (7), 429–439.
Houlsby, G.T., Amorosi, A., Rollo, F., 2019. Non-linear anisotropic hyperelasticity for granular materials. Comput. Geotech. 115, 103167.
Irani, N., Salimi, M., Golestaneh, P., et al., 2024. Deep learning-based analysis of true triaxial DEM simulations: Role of fabric and particle aspect ratio. Comput. Geotech. 173, 106529.
Jamiolkowski, M., Kongsukprasert, L., Lo Presti, D., 2004. Characterization of gravelly geomaterials. Proceedings of the fifth international geotechnical conference 2, 29–56.
Jiang, M.J., Yang, J., 2024. Small-strain Young's modulus of granular materials at anisotropic stress states: a 3D DEM study. Powder Technol. 448, 120249.
Kruyt, N.P., Agnolin, I., Luding, S., et al., 2010. Micromechanical study of elastic moduli of loose granular materials. J. Mech. Phys. Solids 58 (9), 1286–1301.
Kuhn, M.R., Sun, W.C., Wang, Q., 2015. Stress-induced anisotropy in granular materials: fabric, stiffness, and permeability. Acta Geotech. 10 (4), 399–419.
Kuwano, R., Jardine, R.J., 2002. On the applicability of cross-anisotropic elasticity to granular materials at very small strains. Géotechnique 52 (10), 727–749.
Kuwano, R., Jardine, R.J., 2007. A triaxial investigation of kinematic yielding in sand. Géotechnique 57 (7), 563–579.
Liao, C.L., Chang, T.P., Young, D.H., et al., 1997. Stress-strain relationship for granular materials based on the hypothesis of best fit. Int. J. Solids Struct. 34 (31–32), 4087–4100.
Lings, M.L., Pennington, D.S., Nash, D.F.T., 2000. Anisotropic stiffness parameters and their measurement in a stiff natural clay. Géotechnique 50 (2), 109–125.
Liu, Y., Zhang, D., Wu, S.C., et al., 2020. DEM investigation on the evolution of fabric under true triaxial conditions in granular materials. Int. J. Geomech. 20 (8), 04020110.
Liu, Y., Yan, Z.Y., 2025. Particle size effect on the evolution of stress and fabric in granular materials under true triaxial conditions. Int. J. Geomech. 25 (4), 04025043.
Love, A.E.H., 2013. A treatise on the mathematical theory of elasticity. Cambridge University Press, Cambridge.
Mindlin, R.D., Deresiewicz, H., 1953. Elastic spheres in contact under varying oblique forces. J. Appl. Mech. 20 (3), 327–344.
Otsubo, M., Li, Y., Kuwano, R., et al., 2025. Contact-scale insights into the shear stiffness of non-spherical granular materials. Géotechnique 75 (11), 1445–1456.
Payan, M., Senetakis, K., Khoshghalb, A., et al., 2017. Effect of gradation and particle shape on small-strain Young's modulus and Poisson's ratio of sands. Int. J. Geomech. 17 (5), 04016120.
Satake, M., 1982. Fabric tensor in granular materials. In: Vermeer, P.A., Luger, H.J. (Eds.), IUTAM Symposium on Deformations and Failure of Granular Materials. Balkema, Rotterdam, pp. 63–68.
Shi, J.S., Guo, P.J., 2018. Fabric evolution of granular materials along imposed stress paths. Acta Geotech. 13 (6), 1341–1354.
Singh, S., Buscarnera, G., 2024. Deciphering how the particle shape modulates the elastic anisotropy of granular media. Comput. Geotech. 176, 106773.
Singh, S., Buscarnera, G., 2025. Examining the adaptive elastic anisotropy of granular materials. Géotechnique 75 (5), 673–685.
Suwal, L.P., Kuwano, R., 2013. Statically and dynamically measured Poisson's ratio of granular soils on triaxial laboratory specimens. Geotech. Test. J. 36 (4), 493–505.
Thornton, C., 2000. Numerical simulations of deviatoric shear deformation of granular media. Géotechnique 50 (1), 43–53.
Wen, Y.X., Zhang, Y.D., 2022. Relation between void ratio and contact fabric of granular soils. Acta Geotech. 17 (10), 4297–4312.
Yimsiri, S., Soga, K., 2000. Micromechanics-based stress-strain behaviour of soils at small strains. Géotechnique 50 (5), 559–571.
Yimsiri, S., Soga, K., 2011. Cross-anisotropic elastic parameters of two natural stiff clays. Géotechnique 61 (9), 809–814.
Zhao, J., Guo, N., 2015. The interplay between anisotropy and strain localisation in granular soils: a multiscale insight. Géotechnique 65 (8), 642–656.

Zhou, H.C., Gu, X.Q., Hu, J., 2026a. Investigating the nonlinear stiffness of granular materials: a DEM perspective on stress path dependence. Int. J. Numer. Anal. Meth. Geomech. 50, 260–280.
Zhou, H.C., Gu, X.Q., Liang, X.M., 2026b. Deciphering the role of anisotropy in elastic incremental behavior and path-dependent shear stiffness of granular materials. Comput. Geotech. 193, 107953.
Zhou, H.C., Gu, X.Q., Liang, X.M., et al., 2026c. Difference between static and dynamic small strain shear stiffness of anisotropic granular materials: a DEM study. Soil Dyn. Earthq. Eng. 200, 109822.
Zhou, W., Yang, S.H., Liu, J.Y., et al., 2022. Effect of inter-particle friction on 3D accordance of stress, strain, and fabric in granular materials. Acta Geotech. 17 (7), 2735–2750.